Monthly Notices
of the
ROYAL ASTRONOMICAL SOCIETY

MNRAS **461,** 1816–1840 (2016)
Advance Access publication 2016 June 21

doi:10.1093/mnras/stw1411

Extended Lyα emission around quasars with eclipsing damped Lyα systems

H. Fathivavsari,[1⋆] P. Petitjean,[1⋆] P. Noterdaeme,[1⋆] I. Pâris,[2] H. Finley,[3,4] S. López[5] and R. Srianand[6]

[1]*Institut d'Astrophysique de Paris, Université Paris 6-CNRS, UMR7095, 98bis Boulevard Arago, F-75014 Paris, France*
[2]*Osservatorio Astronomico di Trieste, via G. B. Tiepolo 11, I-34131 Trieste, Italy*
[3]*CNRS/IRAP, 14 Avenue E. Belin, F-31400 Toulouse, France*
[4]*University Paul Sabatier of Toulouse/ UPS-OMP/ IRAP, F-31400 Toulouse, France*
[5]*Departamento de Astronomía, Universidad de Chile, Casilla 36-D, Santiago, Chile*
[6]*Inter-University Centre for Astronomy and Astrophysics, Post Bag 4, Ganeshkhind, 411 007 Pune, India*

Accepted 2016 June 9. Received 2016 June 6; in original form 2016 April 12

ABSTRACT

We present spectroscopic observations of six high redshift ($z_{\rm em} > 2$) quasars, which have been selected for their Lyman α (Lyα) emission region being only partially covered by a strong proximate ($z_{\rm abs} \sim z_{\rm em}$) coronagraphic damped Lyα system (DLA). We detected spatially extended Lyα emission envelopes surrounding these six quasars, with projected spatial extent in the range $26 \leq d_{\rm Ly\alpha} \leq 51$ kpc. No correlation is found between the quasar ionizing luminosity and the Lyα luminosity of their extended envelopes. This could be related to the limited covering factor of the extended gas and/or due to the AGN being obscured in other directions than towards the observer. Indeed, we find a strong correlation between the luminosity of the envelope and its spatial extent, which suggests that the envelopes are probably ionized by the AGN. The metallicity of the coronagraphic DLAs is low and varies in the range $-1.75 < {\rm [Si/H]} < -0.63$. Highly ionized gas is observed to be associated with most of these DLAs, probably indicating ionization by the central AGN. One of these DLAs has the highest Al III/Si II ratio ever reported for any intervening and/or proximate DLA. Most of these DLAs are redshifted with respect to the quasar, implying that they might represent infalling gas probably accreted on to the quasar host galaxies through filaments.

Key words: quasars: absorption lines – quasars: emission lines – quasars: general.

1 INTRODUCTION

The study of the gas associated with quasars, either in the disc or halo of the host galaxy is important in understanding the interplay between the AGN, its host-galaxy and the galactic environment. Linking the quasar host galaxy to the intergalactic medium (IGM), the circum-galactic medium (CGM) may provide fuel for star formation activities in the host galaxy. Indeed, gas from the IGM is being accreted along filaments through cold streams on to quasar host galaxies (Cantalupo et al. 2014; Martin et al. 2014). In addition, the enrichment of the IGM by strong starburst- and/or AGN-driven outflows also occurs through the CGM gas (Adelberger et al. 2005; D'Odorico et al. 2013; Shull et al. 2015, Bordoloi et al. 2016). If strong enough, these outflows can expel a large fraction of gas from the CGM into the IGM and consequently suppress further star formation in the galaxy (Silk & Rees 1998; Maiolino et al. 2012). Observing the CGM around high redshift quasars will hence offer important insights into the so-called AGN feedback in galaxy formation and evolution.

For decades, the preferred observational technique for studying the CGM has been the analysis of absorption lines detected in the spectra of background quasars (Bahcall & Spitzer 1969; Petitjean et al. 1996a; Croft et al. 2002; D'Odorico, Petitjean & Cristiani 2002; Bergeron et al. 2004; Hennawi et al. 2006; Hennawi & Prochaska 2007; Steidel et al. 2010; Churchill et al. 2013; Landoni et al. 2016; Péroux et al. 2016; Quiret et al. 2016). This observational technique revealed the presence of infalling and outflowing absorbing material around high redshift galaxies (Steidel et al. 2000; Simcoe, Sargent & Rauch 2004; Bouché et al. 2007; Ryan-Weber et al. 2009; Rubin et al. 2012; Shull, Danforth & Tilton 2014). While most of the studies used quasars as background sources, the method has been extended to using galaxies (e.g. Steidel et al. 2010) as well

⋆ E-mail: h.fathie@gmail.com (HF); ppetitje@iap.fr (PP); noterdaeme@iap.fr (PN)

as GRBs (e.g. Petitjean & Vergani 2011) as background sources. However, the one-dimensional nature of this method does not allow one to map the spatial distribution of these material around an individual galaxy.

Alternatively, detecting the CGM in emission (e.g. Lyα) around high redshift quasars could in principle provide information on the spatial distribution of the gas surrounding the quasar host galaxies (see Cantalupo et al. 2014; Hennawi et al. 2015). Indeed, extended Lyα emission have been found around high redshift ($z > 2$) quasars, extending up to distances as large as 100–200 kpc with typical luminosity of 10^{43} erg s^{-1} (Hu & Cowie 1987; Heckman et al. 1991a, Heckman et al.1991b; Petitjean et al. 1996b; Lehnert & Becker 1998; Christensen et al. 2006, hereafter CJ06; Courbin et al. 2008; North et al. 2012, hereafter NC12; Borisova et al. 2016). In an effort to study extended Lyα emission around high redshift quasars, Arrigoni Battaia et al. (2016) obtained 15 deep ($\sim$2.0 $\times$ 10^{-18} erg s^{-1} cm^{-2} arcsec^{-2}) narrow band images of $z_{\rm em} \sim 2.25$ quasars, using GMOS on Gemini-South telescope. They detect Lyα emission around half of their quasars, extending up to 32 kpc with a surface brightness in excess of 10^{-17} erg s^{-1} cm^{-2} arcsec^{-2}. Several mechanisms have been proposed to power this emission: photoionization by the photons emitted by an AGN and/or a starburst region (Weidinger, Møller & Fynbo 2004; Weidinger et al. 2005), ionization induced by the shock waves from radio jets (e.g. Heckman et al. 1991a, Heckman et al.1991b), and cooling radiation after the gravitational collapse (a.k.a cold accretion, Haiman, Spaans & Quataert 2000; Yang et al. 2006).

In the 'cold accretion' scenario, a spatially extended distribution of infalling cold gas collapses into the potential wells of dark matter and gets heated. The heat is then dissipated through the emission of Lyα photons. The resulting line radiation could potentially be observed as extended, low surface brightness Lyα 'fuzz' around high redshift quasars (Fardal et al. 2001; Haiman et al. 2000). Based on hydrodynamical simulations of galaxy formation, Dijkstra & Loeb (2009) showed that this infall of primordial gas into the centres of dark matter haloes could explain the observed Lyα emission if only $\gtrsim$10 per cent of the gravitational potential energy is converted into the Lyα radiation. Here, the emission would come from the filamentary cold streams of metal-poor intergalactic gas. The gas is optically thick and self-shielded against external ionizing radiation sources and therefore the emission would not depend on the presence of a central AGN or a starburst region. Haiman & Rees (2001), on the other hand, estimated that if a central quasar is switched on inside a collapsing primordial gas, this could significantly enhance the Lyα emission of the cloud. They predict angular diameter of a few arcseconds and surface brightness $\sim 10^{-18}$ to 10^{-16} erg s^{-1} cm^{-2} arcsec^{-2} for the Lyα fuzz. This surface brightness would be detectable with current telescopes through spectroscopy or deep narrow-band imaging (Steidel, Sargent & Dickinson 1991; Fried 1998; Bergeron et al. 1999; Fynbo, Burud & Møller 2000; Bunker et al. 2003). Confirming the prediction by Haiman & Rees (2001), Weidinger et al. (2004) found low metallicity primordial material falling on to the AGN through the ionizing cone of the quasar, causing the gas to glow in Lyα due to recombination. Moreover, Jiang et al. (2016) found a strong narrow Lyα emission line in the trough of a proximate-DLA (PDLA) towards the quasar SDSS J0952+0114; and they argued that this Lyα emission is most likely originated from some large scale outflowing material driven by the central AGN.

It may well be that the spatially extended Lyα fuzz seen around a high redshift galaxy (hosting a quasar) is powered by more than one powering mechanism at the same time. It is also possible that both infall and outflow of material are occurring simultaneously in the CGM of a single galaxy. Using integral field spectroscopy to study the giant Lyα nebula around a high redshift radio galaxy at $z = 4.11$, Swinbank et al. 2015) found two blueshifted (with respect to the systemic redshift of the galaxy) H I absorbers with covering fraction ~ 1 against the Lyα emission. They argued that the more blueshifted absorber, showing dynamics similar to that of the emitting gas, is part of an expanding shell of gas that surrounds the Lyα emission nebula. They then suggested that the emission nebula itself is probably powered by the cooling of primordial gas inside a dark matter halo. In principle, combining the information from both the 1D and 2D spectra of an Lyα emission envelope would allow one to determine which powering mechanism is at play (Weidinger et al. 2005).

With the aim of accessing spatially extended Lyα emission regions around high redshift quasars, we recently searched the SDSS-III Baryon Oscillation Spectroscopic Survey (BOSS; Dawson et al. 2013) for strong damped Lyα absorption systems (DLAs; log $N_{\rm H\,I} > 21.30$) coincident in redshift with the quasar (Finley et al. 2013). Each of these 'eclipsing DLAs' plays the role of a natural coronagraph, completely extinguishing the broad Lyα emission from the quasar, revealing some narrow Lyα emission line in its trough (Hennawi et al. 2009; Finley et al. 2013; Fathivavsari et al. 2015, hereafter Paper I; Jiang et al. 2016). This narrow emission line originates from a source located at approximately the same redshift as the quasar and possibly physically associated with it. Lyα emission from the quasar narrow line region (NLR), or from star-forming regions in the quasar host galaxy, and Lyα emitting haloes around the quasar could be responsible for this narrow Lyα emission line seen in the DLA trough.

In Finley et al. (2013), we found 26 quasars with $z > 2$, showing narrow Lyα emission line in the trough of their eclipsing DLAs. We then performed follow-up observations of six of these systems using the Magellan-MagE echelle spectrograph in order to gain insight into the origin of their extended emission. One of these six objects (i.e. J0823+0529) was already studied in detail in Paper I and the remaining objects are covered in this paper.

Observations and data reduction are described in Section 2. The properties of individual objects are discussed in Section 3. Results are given in Section 4, and Section 5 presents the conclusions. In this work, we use a standard flat ΛCDM cosmology with $\Omega_\Lambda = 0.73$, $\Omega_m = 0.27$, and $H_0 = 70$ km s^{-1} Mpc^{-1} (Komatsu et al. 2011).

2 OBSERVATIONS AND DATA REDUCTION

In the course of a survey for DLA systems having redshifts coincident with the redshift of the quasar (eclipsing DLAs), we found 26 quasars that exhibit Lyα emission at the bottom of their eclipsing DLAs (Finley et al. 2013). We then performed follow-up echelle spectroscopy of six of these quasars using the Magellan Echellete spectrograph (MagE; Marshall et al. 2008) on the 6.5 m Clay telescope located at Las Campanas observatory in Chile. The spectrograph is equipped with 10 arcsec long slits of various widths and has a medium resolution (R $\sim$ 4000), covering the full visible spectral range (3000–10 000 Å). For one of the quasars (i.e. J0953+0349), we also have an XSHOOTER spectrum (as a part of ESO programme 091.A-0299(A)). The XSHOOTER spectrograph (Vernet et al. 2011), mounted on the Very Large Telescope (VLT), covers the full spectral region from 3000 Å to 2.5 μm and has a resolution of $R \sim 5300$ in the near-infrared (NIR) arm when the slit width is 0.9 arcsec.

Table 1. Journal of MagE observations.

QSO	Date	Exp. time (s) (EW/NS)	Seeing(arcsec) (EW/NS)	Slit width(arcsec) (EW/NS)
J0112−0048	2012-12-13	3600/3600	1.1/1.0	1.0/1.0
J0953+0349	2013-02-13	3600/3600	1.2/1.1	0.85/0.85
J1058+0315	2013-02-13	3600/3600	1.2/1.0	1.0/0.85
J1154−0215	2012-01-22	3017/3600	0.9/0.9	1.0/1.0
J1253+1007	2013-02-13	2700/3600	1.0/1.2	1.0/1.0

The MagE observations were performed by keeping the slit along two perpendicular position angles, namely along north–south and east–west directions. The observations were done in the 'derotator' mode in order to fix the position angles during each exposure time. The journal of the observations is shown in Table 1. For each quasar, the spectrum of a standard star was also obtained, immediately after the science exposure, to allow for a precise flux calibration of the quasar spectra. The spectra were reduced and extracted using the Mage_Reduce pipeline written and developed by George Becker.[1] Since the spectral orders of the observed spectra are curved with respect to the (x,y)-coordinate system defined by the CCD columns and rows (Kelson 2003), we followed the method described in Paper I to rectify the curvature of the orders. The final spectra are then binned with a 3 × 3 box, resulting in FWHM = ∼80 km s^{-1}. Each pixel has a width of ∼ 27 km s^{-1}, and each spectral resolution element is sampled by 3 pixels. Each pixel along the slit covers ∼ 0.3 arcsec. The pipeline uses optimum sky subtraction techniques (Kelson 2003) to subtract the background emission from the 2D spectra. We also checked that the residual flux outside the quasar trace at ∼100 Å away on either side of the extended Lyα emission is consistent with the background noise levels. Therefore, the background subtraction has minimum effect on the extent of the envelopes in our sample.

3 NOTES ON INDIVIDUAL OBJECTS

For each quasar, we determine its systemic redshift, $z_{\rm em}$ (using quasar's intrinsic emission lines like He II, Hβ, C IV,..., etc), the redshift of the eclipsing DLA, $z_{\rm abs}$ (using simultaneous fit of some low ion species), and the redshift of the Lyα emission ($z_{\rm Ly\alpha}$) seen in the trough of the eclipsing DLA. The parameters are listed in Table 2. In this table, columns 8 and 9 are the velocity widths of the Lyα emission ($\Delta V_{\rm Ly\alpha}$) and of the C IV absorption features ($\Delta V_{\rm CIV}$), respectively. The Lyα emission (resp. C IV absorption) velocity width is defined as the wavelength region over which the flux level (resp. optical depth) is larger than the 1σ detection limit. Using VPFIT,[2] we fit the low and high ion species associated with the eclipsing DLAs and then determine the metallicity of the absorbers when possible. To fit the absorption lines we used the same techniques described in Fathivavsari et al. (2013). The plots showing the 1D and 2D emission spectra along with the fits to the absorption lines for the quasar J0112−0048 are presented in Figs 1 and 2 while the corresponding plots of the remaining quasars are shown in Appendix A. The parameters of the fits are summarized in Tables 3 and 4. In Table 3, the values in brackets are uncertain because either the corresponding absorption lines are affected by noise or all lines are strongly saturated.The metallicity and relative abundances given in the last two rows of Table 3 are obtained using solar photospheric abundances from Asplund et al. (2009).

In all quasar spectra, the Lyα emission detected in the trough of the DLA is observed to be spatially extended. One can think of this Lyα emission as a combination of two components: the spatially unresolved narrow Lyα emission (located on the quasar trace) and the second component which extends beyond the quasar trace. The quasar trace is defined by the point spread function (PSF) of the quasar continuum close to the wavelength range where the Lyα emission is detected. The FWHM of the PSF (∼1 arcsec) is approximately 8 kpc at the relevant redshift. To determine the flux of the extended emission, we first need to subtract the contribution from the unresolved component of the emission which is seen on the quasar trace. To do so, we follow the method described in section 5 of Paper I. Throughout this paper, by envelope luminosity we mean the luminosity of the Lyα emission after subtracting that along the quasar trace. The Lyα flux and luminosity of the extended envelopes, their spatial extent, and their mean surface brightness are listed in Tables 5 and 6.

We emphasize that the extent of an envelope along the north, south, east, or west direction is defined as the distance (in arcsec or kpc) from the centre of the quasar trace up to the spatial pixel at which the flux density per square arcsec reaches below the 1σ detection limit. The 1σ uncertainty in the flux for each PA is reported in the sixth column of Table 5.

3.1 SDSS J011226.76−004855.8

For this quasar we detect Lyα, C IV, and He II emission lines. To estimate the quasar redshift, we have fitted a Gaussian function to the He II emission line which resulted in $z_{\rm em} = 2.1485$ (see panel (a) of Fig. 1). We adopt this value as the systemic redshift of the quasar.

Associated with the eclipsing DLA along this line of sight, we detect absorption from low and high ionization species like, O I, C II, Al II, Al III, Mg II, Fe II, Si II, Si IV, and C IV. As shown in panel (c) of Fig. 1, the low-ion absorption profiles are dominated by a single component at $z_{\rm abs} = 2.1493$. The DLA is located at v ∼ +76 km s^{-1} relative to the quasar. We used several Fe II transitions (i.e. Fe IIλ2600, 2382, 2344, and 2260) to constrain the Doppler parameter of this component. In panel (b) of Fig. 1, the VPFIT solutions for different Doppler parameters are shown by different colours.

The fact that Fe IIλ2260 is detected and is not saturated allows us to constrain the Doppler parameter. As shown in panel (b) of Fig. 1, the best fit of the four Fe II transitions results in $b = 17.4$ km s^{-1}. To determine the H I column density of the DLA, a single component fit was conducted to the DLA trough with the redshift fixed to the value derived from the low-ion species, i.e. $z_{\rm abs} = 2.1493$, and we obtained log $N_{\rm HI} = 21.95 \pm 0.10$. The fit is shown in panel (d) of Fig. 1 as a red curve overplotted on the observed spectrum (black curve), with the two green curves indicating the corresponding ±1σ uncertainty. The fit to other low-ion species was performed by fixing their corresponding Doppler parameter and redshift to those obtained for Fe II. The C IV and Si IV doublets were fitted independently with all parameters allowed to vary during the fitting process. The parameters of the fit are listed in Tables 3 and 4. As shown in panel (c) of Fig. 1, the expected position of the N V doublet falls on the red wing of the strong DLA profile and is probably lost in the noise. The Si IVλ1402 absorption profile is also blended with some unidentified features. The C IV doublet has two absorption components located at v ∼ +5 and −117 km s^{-1} relative to $z_{\rm abs}$. While the component at v ∼ +5 is also seen in Si IV, the second component is

[1] ftp://ftp.ast.cam.ac.uk/pub/gdb/mage_reduce/
[2] http://www.ast.cam.ac.uk/∼rfc/vpfit.html

Table 2. The redshifts of the quasar, the Lyα emission, and the DLA are given in columns 2–4 and the corresponding velocity separations are in columns 5–7. The values in columns 5 and 6 are with respect to the quasar's adopted systemic redshift while the values in column 7 are relative to the DLA redshift, i.e. z_{abs}. Columns 8 and 9 give the velocity widths of the extended Lyα emission and the C IV absorption profile where the signal is more than the 1σ detection limit. Note that all velocities are in km s^{-1}. The last column gives the upper limit (in pc) on the size of the H I cloud derived by assuming that the hydrogen number density in our eclipsing DLAs is $n_H > 10$ cm^{-3} (see Section 4.6.2).

ID	z_{em}	$z_{Ly\alpha}$	z_{abs}	$\delta V_{DLA\text{-}QSO}$	$\delta V_{Ly\alpha\text{-}QSO}$	$\delta V_{Ly\alpha\text{-}DLA}$	$\Delta V_{Ly\alpha}$	ΔV_{CIV}	l(H I)
J0112−0048	2.1485	2.1482	2.1493	+76	−29	−105	800	320	<289
J0823+0529	3.1875	3.1925	3.1910	+250	+358	−107	1400	754	<10[a]
J0953+0349	2.5940	2.5929	2.5961	+175	−92	−267	1222	837	<289
J1058+0315	2.3021	2.3029	2.2932	−809	+73	+882	520	240	<204
J1154−0215	2.1810	2.1842	2.1853	+405	+301	−103	1157	1064	<182
J1253+1007	3.0150	3.0308	3.0312	+1207	+1177	−30	1560	1030	<65

Note. [a]See Paper I.

Table 3. Column densities and metallicities of the low-ionization species detected in the eclipsing DLAs. The values in brackets are uncertain because either the corresponding absorption lines are affected by noise or all lines are strongly saturated. Column densities are given in logarithmic units.

	J0112−0048	J0823+0529	J0953+0349	J1058+0315	J1154−0215	J1253+1007
b[a]	17.4	20.0	20.0	15.0	20.0	37.0
N(O I)	[17.47 ± 0.24]	[17.08 ± 0.50]	[17.11 ± 0.20]	.....	.....	16.04 ± 0.10
N(Si II)	16.83 ± 0.14	16.42 ± 0.10	15.71 ± 0.10	15.90 ± 0.20	15.55 ± 0.20	15.36 ± 0.10
N(Fe II)	15.05 ± 0.20	15.33 ± 0.20	15.43 ± 0.20	15.74 ± 0.15	15.35 ± 0.20	14.27 ± 0.10
N(C II)	.....	.....	[17.11 ± 0.20]	.....	.....	[16.12 ± 0.20]
N(C II*)	.....	.....	[15.70 ± 0.20]	.....	.....	[14.80 ± 0.20]
N(Al II)	[14.77 ± 0.20]	.....	[14.09 ± 0.15]	[15.56 ± 0.16]	[15.30 ± 0.30]	[13.69 ± 0.10]
N(Al III)	13.91 ± 0.10	14.80 ± 0.10	13.65 ± 0.10	13.36 ± 0.10	15.20 ± 0.30	13.14 ± 0.10
N(Mg II)	[15.90 ± 0.25]	.....	.....	16.96 ± 0.20	[15.30 ± 0.30]	.....
N(H I)	21.95 ± 0.10	21.70 ± 0.10	21.95 ± 0.10	21.80 ± 0.10	21.75 ± 0.10	21.30 ± 0.10
[Si/H]	−0.63	−0.79	−1.75	−1.41	−1.71	−1.45
[Si/Fe]	1.77	1.08	0.27	0.15	0.19	1.08

Note. [a]Doppler parameter (km s^{-1}), see the text.

only detected in C IV, and no low-ion absorption is associated with this second component.

As shown in Fig. 2, the Lyα emission at the centre of the DLA trough is spatially extended along both PAs. Along the north–south (NS) direction, the emission is more extended to the north up to ∼3.5 arcsec (30 kpc) while the extension to the south reaches up to ∼1.6 arcsec (13.5 kpc) away from the quasar trace. Along the east–west direction, the emission seems to be more extended to the west (∼3 arcsec or 25.5 kpc) than to the east (∼2 arcsec or 16.5 kpc). The Lyα flux and luminosity of the envelope, its angular size, and the mean surface brightness are listed in Tables 5 and 6.

From panel (c) of Fig. 2, one can see that the Lyα emission on the quasar trace is asymmetric, with a steeper drop of the flux in its red wing and a shallower rise in the blue wing. This asymmetry is less prominent along the east–west (EW) direction due to the high level of noise. Since the emission seen on the trace is not resolved, one would expect the same spectrum for the quasar trace, regardless of the slit orientation. As illustrated in panel (c) of Fig. 2, the spectra on the trace for the two PAs are consistent within the errors.

The Lyα emitting (resp. absorbing) gas is ∼29 km s^{-1} (resp. ∼76 km s^{-1}) blueshifted (resp. redshifted) relative to the systemic redshift of the quasar. These low velocity differences hint at the possibility that the emitting and/or absorbing cloud may originate from somewhere in the quasar host galaxy or its close vicinity.

3.2 SDSS J095307.13+034933.8

This is the only quasar for which we also have an XSHOOTER spectrum. Unfortunately, the SNR of this spectrum in the regions where we expect to see redshifted Mg II, [O II] and [O III] emission lines is not very high because the lines are either located in bad portions of the spectrum or spoiled by strong sky lines. However, we could still use the Hβ emission line to get an emission redshift of $z_{em} = 2.5940$ (see Fig. A1). We adopt this redshift as the systemic redshift of the quasar. As shown in Fig. A1, we also detect O Iλ1304, C III]λ1909, Si III]λ1892, and C IVλ1548 emission lines in the MagE spectrum of this quasar. Fitting Gaussians to these emission lines yields z = 2.5930, 2.5883, 2.5915, and 2.5880, respectively. The emission redshift from O Iλ1304 and Si III]λ1892 are consistent with that obtained from Hβ within 200 km s^{-1}. But C III] and C IV emission lines show, respectively, 475 and 500 km s^{-1} blueshift with respect to the adopted systemic redshift of the quasar.

We fit a single Gaussian to the low ionization lines to get the redshift $z_{abs} = 2.5961$ of the eclipsing DLA along this line of sight which is 175 km s^{-1} redshifted with respect to the quasar. We fit the Lyα trough with a Voigt profile and derived log N_{HI} = 21.95 ± 0.10. We detect absorption from O I, C II, Si II, Al II, Fe II in one component (see Fig. A1). To constrain the corresponding Doppler parameter, we follow the same procedure described in the previous section. As demonstrated in panel (b) of Fig. A1, Doppler parameters less than 20 km s^{-1} (pink and blue curves) are clearly excluded while larger Doppler parameters (i.e. $b > 25$ km s^{-1}) are consistent with the observations. Therefore, our reported column densities and metallicity should be considered as upper limits. Parameters of the fit are reported in Tables 3 and 4, and the metallicity of the system is [Si/H] < −1.75 ± 0.20.

It is interesting to note that strong low ionization components (O I and C II, C II*) are also seen at $z = 2.5882$ (660 km s^{-1} blueshifted

Table 4. Column densities of high ionization species. Note that the second column gives the velocity separation of that component with respect to the strongest component in the low-ion species (see Table 2).

z	δV(km s^{-1})	Ion(X)	b(km s^{-1})	logN(X)
		SDSS J0112−0048		
2.148066	−117.5	C IV	10.0 ± 2.0	15.67 ± 0.30
2.149356	+5.3	C IV	16.7 ± 5.0	16.70 ± 0.30
2.149338	+3.6	Si IV	56.1 ± 4.0	13.86 ± 0.20
		SDSS J0953+0349		
2.585898	−851.7	C IV	22.2 ± 9.0	14.24 ± 0.24
2.588245	−665.6	C IV	68.8 ± 7.7	15.06 ± 0.04
2.590421	−473.8	C IV	62.5 ± 24.0	15.04 ± 0.12
2.591778	−360.5	C IV	10.0 ± 5.0	15.72 ± 0.30
2.593449	−221.1	C IV	40.0 ± 8.7	14.00 ± 0.04
2.595836	−22.0	C IV	41.9 ± 5.4	14.65 ± 0.05
2.588187	−660.4	Si IV	26.4 ± 7.0	14.92 ± 0.30
2.589003	−592.2	Si IV	13.0 ± 5.0	13.30 ± 0.30
2.590254	−487.8	Si IV	34.3 ± 14.0	13.90 ± 0.20
2.595963	−11.4	Si IV	29.0 ± 7.8	14.36 ± 0.21
		SDSS J1058+0315		
2.293476	+34.2	C IV	37.4 ± 5.0	14.93 ± 0.20
2.293406	+27.8	Si IV	24.4 ± 2.3	15.50 ± 0.30
		SDSS J1154−0215		
2.177275	−756.3	C IV	84.8 ± 5.3	14.83 ± 0.10
2.178558	−635.2	C IV	74.6 ± 14.1	14.71 ± 0.20
2.185181	−11.2	C IV	46.4 ± 3.3	14.98 ± 0.20
		SDSS J1253+1007		
3.022167	−672.5	C IV	60.4 ± 2.2	14.95 ± 0.05
3.025153	−450.0	C IV	15.0 ± 2.0	13.75 ± 0.11
3.027819	−251.5	C IV	40.0 ± 5.0	16.20 ± 0.13
3.029663	−114.3	C IV	35.0 ± 5.0	14.10 ± 0.15
3.031250	+3.7	C IV	33.0 ± 2.0	15.70 ± 0.10
3.032776	+117.2	C IV	30.0 ± 3.0	13.30 ± 0.10
3.021977	−686.7	Si IV	93.6 ± 12.0	13.30 ± 0.10
3.027811	−252.1	Si IV	45.8 ± 2.0	14.55 ± 0.10
3.031253	+4.0	Si IV	53.5 ± 2.0	14.54 ± 0.10
3.021785	−701.0	N V	40.2 ± 4.0	15.23 ± 0.12
3.023130	−600.7	N V	11.9 ± 4.5	14.73 ± 0.20
3.027967	−240.5	N V	39.4 ± 2.5	14.80 ± 0.10

with respect to the DLA). The C IV and Si IV absorption associated with this component is strong and spread over ∼250 km s^{-1}. N V may also be present but it seems to be strongly blended with some intervening absorption.

As shown in Fig. A2, the Lyα emission at the bottom of the DLA absorption line is extended along both PAs. From this figure, we can see that the Lyα envelope is spatially asymmetric. The emission extends out to a maximum distance of ∼2.4 arcsec (20 kpc) and ∼1.9 arcsec (16 kpc) in the south and east directions, respectively. Note that the emission towards the north is so weak that we take it as a tentative detection.

The spectra of the quasar trace for the two PAs are consistent with each other within the errors (see panel (c) of Fig. A2). The DLA is redshifted by ∼175 km s^{-1} relative to the systemic redshift of the quasar while the Lyα envelope and the second low-ion system (located at $z_{\rm abs} = 2.5882$) are both blueshifted compared to $z_{\rm em}$ by 92 and 484 km s^{-1}, respectively. It seems possible that the low metallicity DLA ([Si/H] < −1.75) is infalling towards the central AGN and that the second low-ion system is part of some outflowing material. It is also possible that both the absorption and emission originate from the same structure. Note that the transverse extensions of both of the two absorbing clouds should be small compared to the NLR.

3.3 SDSS J105823.73+031524.4

In addition to Lyα, we detect emission from C III], C IV, and He II in the spectrum of this quasar (see Fig. A3). The C III] λ1909 emission line falls on top of a strong sky emission line at 6300 Å and hence cannot yield a reliable redshift estimate. On the other hand, the blue wing of the He II λ1640 emission line is affected by noise. However, we could still use the red wing of the profile to carefully constrain the fit and obtain $z_{\rm em} = 2.3021$ which was adopted as the systemic redshift of the quasar. Interestingly, the C IV emission line indicates a similar redshift.

The broad Lyα emission line of this quasar is extinguished by the presence of a strong DLA located at $z_{\rm abs} = 2.2932$ (derived through simultaneous fit of the low ionization species) which is ∼810 km s^{-1} blueshifted relative to the quasar systemic redshift. The H I column density of log $N_{\rm H\,I} = 21.80 \pm 0.10$ is derived from a single component fit to the DLA profile (see panel (d) of Fig. A3). This DLA is associated with a number of low and high ionization species including O I, C II, Si II, Fe II, Al II, Al III, Mg II, Si IV and C IV (see Fig. A3). The somewhat low SNR of the spectrum does not allow us to uniquely constrain the Doppler parameter using several transitions of the same species. However, we still used four Fe II transitions to derive a lower limit on this parameter, $b > 15$ km s^{-1} (see panel (b) of Fig. A3). We derive iron and silicon abundances of [Fe/H] < −1.56 ± 0.20 and [Si/H] < −1.41 ± 0.20.

Independent fits to the C IV and Si IV absorption lines were conducted with one main component (see Fig. A3). A Gaussian fit to the Lyα emission line gives $z_{\rm Ly\alpha} = 2.3029$ which is only ∼73 km s^{-1} redshifted with respect to the systemic redshift of the quasar. The striking feature in Fig. A3 is that the DLA is ∼880 km s^{-1} blueshifted with respect to the Lyα emission. This is the largest velocity separation seen between the DLA and the narrow Lyα emission line in our sample. This is also the largest separation between the DLA and the quasar. This large velocity offset suggests that the Lyα emission may be associated with the quasar and not the DLA.

Although SNR is not very high, we note that the flux on the trace derived by our decomposition is smaller along PA = NS compared to PA = EW (see panel (c) of Fig. A4). Actually, the slit width for the two PAs are not the same: 0.8 and 1.0 arcsec for PA = NS and PA = EW, respectively. This is because the seeing was better for PA = NS. We also note that a point-like source is present on the 2D spectrum at PA = EW at the velocity of ∼50 km s^{-1} relative to the quasar (see panel (a) of Fig. A4). We believe that this point-source is contributing to the flux on the trace. This source is not seen along PA = NS because of the better seeing and smaller slit-width.

If we assume that this point-like source of Lyα emission arises from a star-forming region inside a foreground (or the host) galaxy, we can estimate the star formation rate (SFR) implied by its Lyα luminosity. Integrating over the region where this compact emission is detected, we derive a flux of $f = 3.26 \times 10^{-17}$ erg s^{-1} cm^{-2}, with corresponding Lyα luminosity of $L = 1.40 \times 10^{42}$ erg s^{-1}. Assuming the standard case B recombination theory and using the relation proposed by Kennicutt (1998), we get SFR = 1.3 $M_\odot$ yr^{-1}. This is a lower limit to the SFR as, in addition to the slit loss, dust extinction and/or absorption by foreground neutral hydrogen could diminish the actual Lyα flux radiated away from the galaxy.

Table 5. Derived parameters of emission lines. First column: slit position angles. Second column: spatial extent of the Lyα emission (i.e. the diameter) of the envelope in both arcsec and kpc. Third column: flux of the unresolved region which is seen on the quasar trace. Fourth column: flux of the extended Lyα envelope which is seen beyond the quasar trace. Fifth column: 3σ detection limit (DL) of the Lyα emission envelope outside the quasar trace. Sixth column: 1σ uncertainty in the Lyα surface brightness. Seventh column: integrated flux over the expected He II emission line region outside the quasar trace. Eighth column: 3σ detection limit of the He II emission envelope outside the quasar trace. Ninth column: 3σ upper limit He II/Lyα ratio determined from the values given in the eighth and fourth columns.

PA	Extent (''; kpc)	NEL flux (Lyα) [erg s^{-1} cm^{-2}]	Envlp. flux (Lyα) [erg s^{-1} cm^{-2}]	3σ DL$_{Ly\alpha}$[a] [erg s^{-1} cm^{-2}]	1σ uncertainty[b] [erg s^{-1} cm^{-2} arcsec^{-2}]	Envlp. flux (He II)[c] [erg s^{-1} cm^{-2}]	3σ DL$_{HeII}$[c] [erg s^{-1} cm^{-2}]	Flux ratio (He II/Lyα)
				SDSS J0112−0048				
NS	(5.1; 43)	$2.54(\pm0.10)\times10^{-16}$	$1.04(\pm0.12)\times10^{-16}$	4.46×10^{-17}	0.92×10^{-17}	1.65×10^{-18}	2.01×10^{-17}	<0.19
EW	(4.9; 42)	$2.46(\pm0.37)\times10^{-16}$	$2.53(\pm0.44)\times10^{-16}$	1.36×10^{-16}	3.55×10^{-17}	6.42×10^{-18}	1.69×10^{-17}	<0.07
				SDSS J0823+0529				
NS	(5.5; 42)	$3.59(\pm0.10)\times10^{-16}$	$3.97(\pm0.10)\times10^{-16}$	4.05×10^{-17}	0.74×10^{-17}	1.22×10^{-17}	2.21×10^{-17}	<0.06
EW	(6.0; 46)	$3.36(\pm0.10)\times10^{-16}$	$2.68(\pm0.10)\times10^{-16}$	4.15×10^{-17}	0.92×10^{-17}	1.24×10^{-17}	2.04×10^{-17}	<0.08
				SDSS J0953+0349				
NS	(3.6; 30)	$1.27(\pm0.12)\times10^{-16}$	$0.52(\pm0.11)\times10^{-16}$	4.08×10^{-17}	0.93×10^{-17}	8.47×10^{-18}	3.73×10^{-17}	<0.71
EW	(3.1; 26)	$1.22(\pm0.10)\times10^{-16}$	$0.54(\pm0.10)\times10^{-16}$	3.41×10^{-17}	1.15×10^{-17}	6.70×10^{-18}	3.06×10^{-17}	<0.57
				SDSS J1058+0315				
NS	(3.7; 31)	$0.70(\pm0.19)\times10^{-16}$	$0.65(\pm0.20)\times10^{-16}$	4.39×10^{-17}	1.59×10^{-17}	7.82×10^{-18}	1.78×10^{-17}	<0.27
EW	(4.1; 35)	$1.11(\pm0.18)\times10^{-16}$	$1.15(\pm0.17)\times10^{-16}$	5.42×10^{-17}	1.80×10^{-17}	7.35×10^{-18}	2.18×10^{-17}	<0.19
				SDSS J1154−0215				
NS	(6.0; 51)	$1.19(\pm0.10)\times10^{-16}$	$1.01(\pm0.10)\times10^{-16}$	3.91×10^{-17}	0.53×10^{-17}	6.24×10^{-18}	2.11×10^{-17}	<0.21
EW	(5.4; 46)	$1.23(\pm0.15)\times10^{-16}$	$1.82(\pm0.15)\times10^{-16}$	4.51×10^{-17}	1.03×10^{-17}	3.47×10^{-18}	2.22×10^{-17}	<0.12
				SDSS J1253+1007				
NS	(6.4; 51)	$2.66(\pm0.18)\times10^{-16}$	$2.26(\pm0.21)\times10^{-16}$	5.93×10^{-17}	1.32×10^{-17}	1.75×10^{-17}	4.07×10^{-17}	<0.18
EW	(4.9; 39)	$2.62(\pm0.15)\times10^{-16}$	$2.34(\pm0.18)\times10^{-16}$	6.23×10^{-17}	1.77×10^{-17}	2.37×10^{-17}	4.45×10^{-17}	<0.19

Notes. [a]The 3 σ detection limit is calculated from the standard deviation (in the flux) of the spectral and spatial pixels over which the Lyα emission outside the quasar trace is detected.
[b]The 1σ uncertainty in the flux is used to determine the spatial extent of the Lyα envelope.
[c]Since the He II emission envelopes are apparently not detected outside the quasar trace in all our spectra, the integration is performed over the same spectral and spatial extent as the corresponding Lyα emission envelope.

Table 6. The Lyα flux (erg s^{-1} cm^{-2}), luminosity (erg s^{-1}) and surface brightness (SB; erg s^{-1} cm^{-2} arcsec^{-2}) of the envelopes detected around the quasars in the sample. Note that the flux and luminosity of the extended envelopes are corrected for the Galactic extinction and the slit-clipping effects (see Text). First row: the ID of the quasars in the sample. Second row: the integrated Lyα flux in the quasars' PSF centred on the trace (i.e. the NEL unresolved luminosity). Third row: the integrated flux in the extended envelopes. Fourth row: the integrated luminosity of the quasars NEL. Fifth row: the luminosity of the extended envelopes. Sixth row: the ionizing luminosity of the quasars, i.e. $L_{<912}$. Seventh row: PCA prediction of the Lyα luminosity of the quasars in the BELR (note that this luminosity is measured in the rest-frame wavelength interval 1200−1230 Å). Eighth row: the mean surface brightness of the envelopes.

ID	J0112−0048	J0823+0529	J0953+0349	J1058+0315	J1154−0215	J1253+1007
$f_{NEL}(\times10^{-16})$	2.82 ± 0.22	7.57 ± 0.20	1.43 ± 0.10	0.83 ± 0.16	1.35 ± 0.10	2.80 ± 0.12
$f_{envlp}(\times10^{-16})$	8.83 ± 1.14	18.77 ± 0.50	2.35 ± 0.33	3.86 ± 0.56	6.71 ± 0.41	10.88 ± 0.67
$L_{NEL}(\times10^{43})$	1.03 ± 0.10	3.61 ± 0.19	0.83 ± 0.10	0.35 ± 0.10	0.51 ± 0.10	2.36 ± 0.10
$L_{envlp}(\times10^{43})$	3.21 ± 0.41	17.88 ± 0.49	1.36 ± 0.19	1.65 ± 0.24	2.54 ± 0.15	9.18 ± 0.56
$L_{<912}(\times10^{44})$	2.12	3.98	6.51	2.31	1.71	8.05
$L_{BLR}(\times10^{44})$	0.60	6.78	2.69	1.12	2.19	2.75
SB$(\times10^{-17})$	4.00 ± 0.50	5.95 ± 0.16	1.91 ± 0.27	3.07 ± 0.45	2.84 ± 0.17	4.71 ± 0.29

Moreover, Erb et al. (2006) showed that, in Lyman break galaxies (LBGs), I(Lyα)/I(Hα) = 0.6. Therefore, if our point-like source is an LBG, this implies a higher SFR of 18.6 $M_\odot$ yr^{-1}. The velocity separation of ∼54 km s^{-1} of this point-like source from the quasar, along with its small impact parameter (∼ 0.5 arcsec or ∼4 kpc) suggests that it might be inside the zone-of-influence of the quasar. Therefore, the observed star formation activity might have been triggered by the strong feedback from the AGN. Alternatively, this compact Lyα emission could have been induced by the quasar through the Lyα fluorescence emission (Srianand et al. 2016).

The 2D spectra of this quasar reveal extended Lyα emission along both PAs (Fig. A4). Along PA = NS, the emission is equally extended up to ∼1.8 arcsec (15.5 kpc) to the north and south directions. A notable feature along PA = EW is that the velocity spread of the emission (∼ 500 km s^{-1}) is similar along the trace and at ∼1.3 arcsec (11 kpc) away from the trace to the west. The emission is also spatially more extended to the west, reaching out to ∼2.4 arcsec (20 kpc). The presence of the point-like source of Lyα emission could in part be responsible for the high velocity extent of the envelope (> 500 km s^{-1}) towards the west.

The eclipsing DLA along this line of sight is ∼810 km s^{-1} blueshifted with respect to z_{em}. The lack of N V and O VI absorption lines and the low metallicity of the absorber argue against a scenario in which the DLA is associated with outflowing interstellar medium from the quasar host. Alternatively, the absorber may arise from a foreground galaxy unrelated to the quasar.

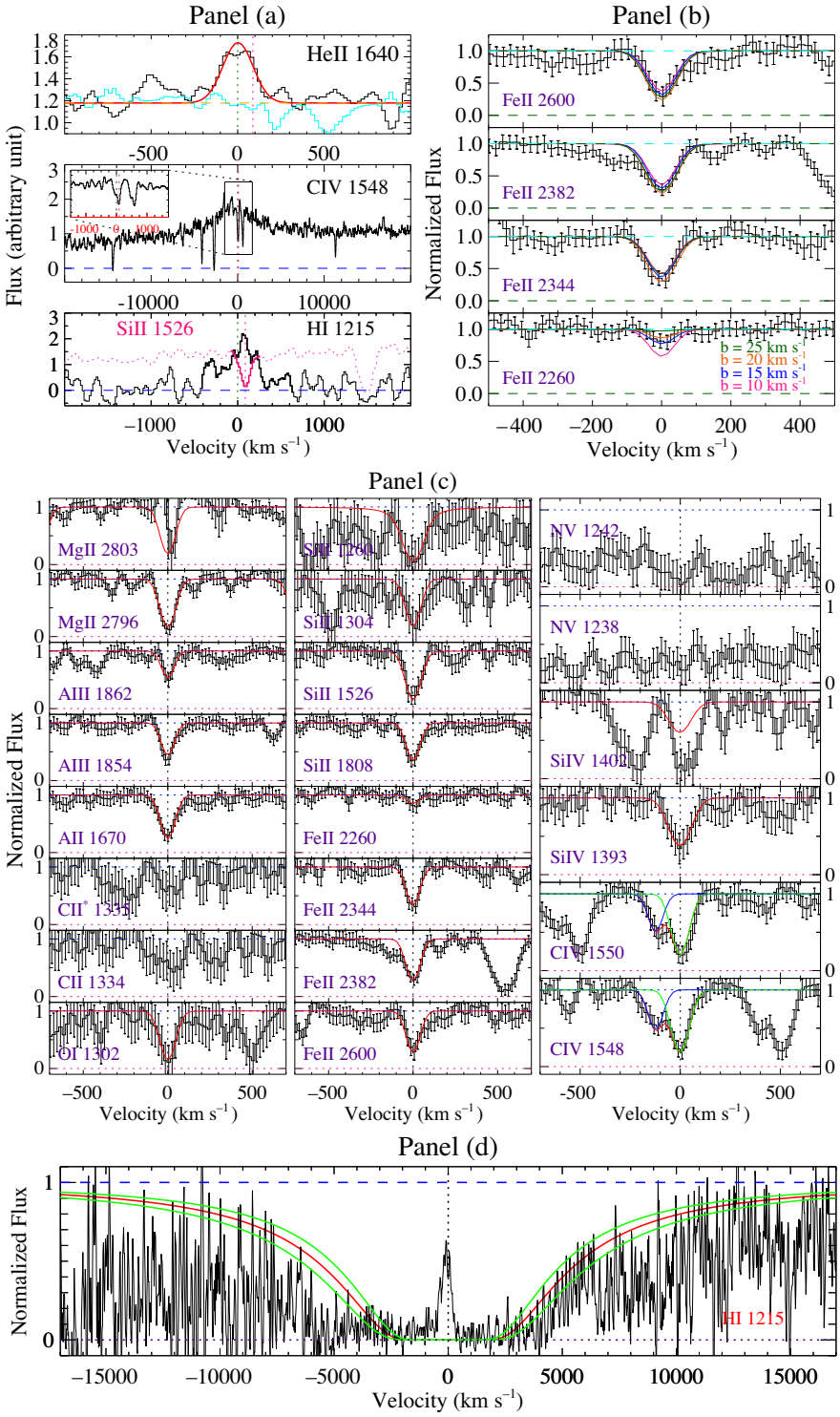

Figure 1. Panel (a): velocity profiles of some emission lines detected in the spectrum of the quasar J0112−0048. The adopted systemic redshift of the quasar ($z_{\rm em} = 2.1485$) is used as the origin of the velocity scale. The sky spectrum is overplotted as a cyan curve in the top sub-panel. The pink vertical dotted lines mark the redshift of the low-ion species. Note that in the H I emission line sub-panel, we overplot the Si IIλ1526 absorption as a pink curve. The inset in the middle sub-panel shows a close-up view of the C IV emission line region. Panel (b): the optical depths of several Fe II transitions are used to constrain the Doppler parameter. The best fits for different Doppler parameters are indicated by different colours. Panel (c): velocity plots and VPFIT solutions (where applicable) of the species detected in the DLA at $z_{\rm abs} = 2.1493$. As shown in the C IV doublet panel, the C IV absorption has an additional weaker component at $v = -117\,{\rm km\,s^{-1}}$. For the low-ion species, we assume $b = 17.4\,{\rm km\,s^{-1}}$ as found from the analysis shown in Panel (b). Panel (d): the red curve is the single component fit to the damped Lyα absorption profile with the two green curves showing the $\pm\,1\sigma$ uncertainty.

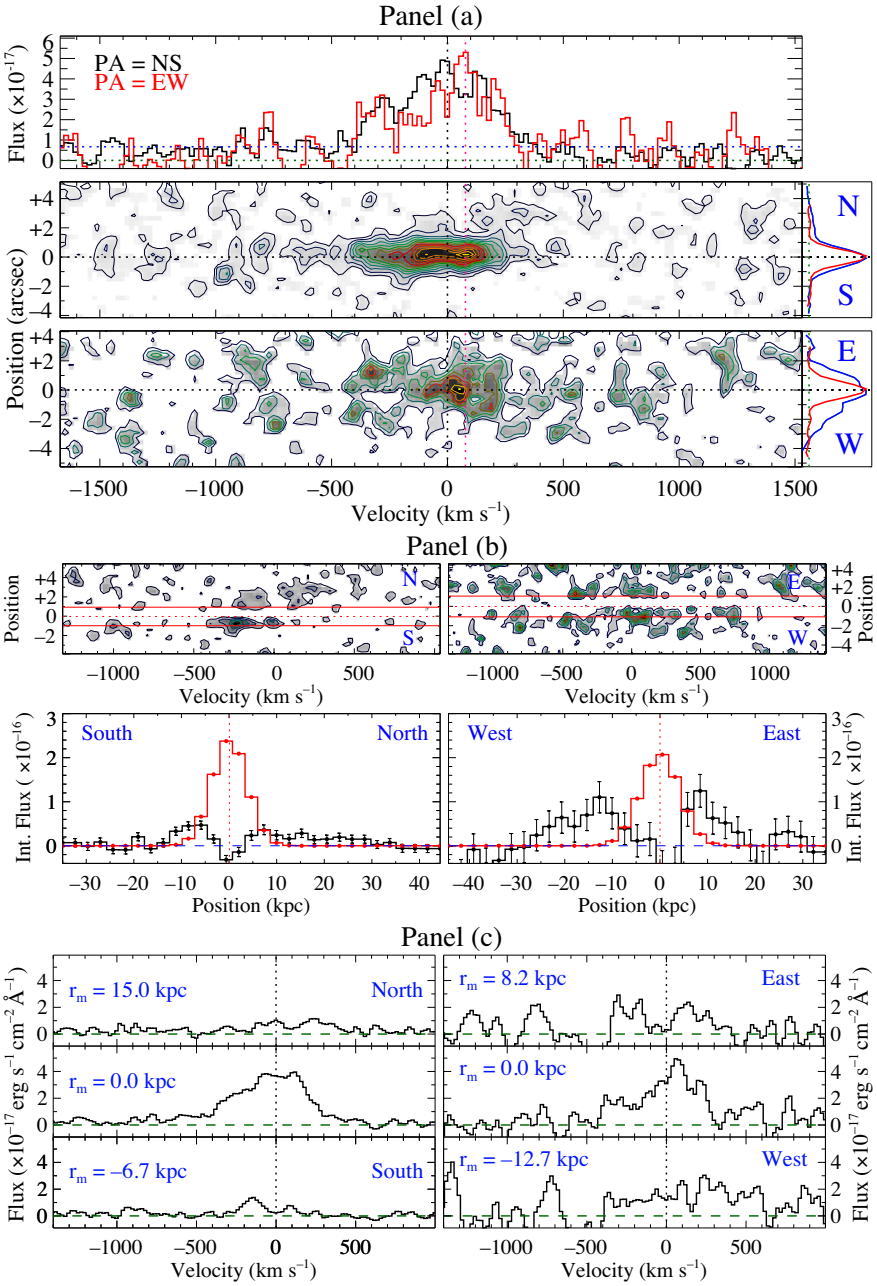

Figure 2. 1D and 2D spectra around the Lyα emission of quasar J0112−0048. Panel (a): this panel comprises of three sub-panels. The zero velocity is at $z_{em} = 2.1485$ and the position of the DLA (at $z_{abs} = 2.1493$) is shown as a vertical pink dotted line in the three sub-panels. The upper sub-panel shows the 1D spectra of the Lyα emission seen at the bottom of the DLA trough for the two PAs. The green and blue horizontal dotted lines show the zero flux level and the 1σ uncertainty on the flux, respectively. Here, the y-axis is in the unit of erg s^{-1} cm^{-2} Å^{-1}. The middle and lower sub-panels show the 2D spectra of the Lyα emission seen in the DLA trough for the two PAs. The outermost contour along PA = NS (resp. PA = EW) corresponds to a flux density of 1.83×10^{-19} (resp. 9.13×10^{-20}) erg s^{-1} cm^{-2} Å^{-1} and each contour is separated by 1.83×10^{-19} (resp. 9.13×10^{-20}) erg s^{-1} cm^{-2} Å^{-1} from its neighbouring contour. The black horizontal dotted lines mark the centre of the quasar trace. Panels on the right show the spatial profiles integrated over the whole spectral width of the Lyα emission (blue curves). The red curves show the profile of the quasar continuum PSF. Panel (b): this panel comprises of two upper sub-panels and two lower sub-panels. The upper sub-panels show the 2D spectra of the Lyα emission after subtracting the quasar trace for the two PAs. The contour levels are the same as in panel (a). The centre of the trace is marked by the red horizontal dotted line and the full width of the trace (i.e. 2 × FWHM) is shown by the red solid horizontal lines. The y-axis here is position in arcsecond. The lower sub-panels show the spatial profiles of the extended Lyα emission (black histogram) and that of the quasar trace (red histogram). Here, the y-axis is in erg s^{-1} cm^{-2} arcsec^{-2}. Panel (c): velocity profiles of the spatially extended Lyα emission at several distances from the AGN. The parameter r_m indicates the mean distance to the central AGN.

3.4 SDSS J115432.67−021537.9

For this quasar, we detect emission lines from C IV λ1548, He II λ1640, Si III] λ1892, and C III] λ1909. To estimate the systemic redshift of the quasar, a single Gaussian is fit to the He II emission line with $z_{em} = 2.1810$. A similar fit to the C III] emission line gives $z = 2.1830$. We adopt the former as the systemic redshift of the quasar because the He II line is a more reliable redshift

indicator. Panel (a) of Fig. A5 shows the emission lines and their Gaussian fits.

Associated with the eclipsing DLA along this line of sight, we detect metal absorption lines from Si II, Fe II, Al II, Al III, Mg I, Mg II, C IV, Si IV, and possibly N V. The spectral regions corresponding to the O I λ1302, C II λ1334, C II* λ1335, and N V λλ1339,1402 absorption lines are strongly affected by noise (see panel (c) of Fig. A5). We use four Fe II absorption lines to derive the redshift of the damped Lyα system ($z_{\rm abs} = 2.1853$). We also tried to constrain the Doppler parameter using some Fe II transitions (see panel (b) of Fig. A5). Following the same approach as in previous sections, one can see that the best b-value to fit the four Fe II transitions is $b \sim 20\,{\rm km\,s^{-1}}$. We adopted this b-value and subsequently fit the other absorption lines. Panel (c) of Fig. A5 illustrates the observed velocity profiles and VPFIT solutions (where applicable) of different species. The parameters are given in Tables 3 and 4. A damped profile fitted to the Lyα absorption line resulted in $\log N_{\rm H\,I} = 21.75 \pm 0.10$. The fit is shown as a red curve in panel (d) of Fig. A5 with the two green curves showing the $\pm 1\sigma$ uncertainty in the H I column density. This DLA is 103 and 405 km s^{-1} blueshifted compared to the Lyα emission and systemic redshift of the quasar, respectively (see panel (a) of Fig. A5 and Table 2). The derived metallicity of this absorber is [Si/H] $= -1.71 \pm 0.20$.

The extended Lyα emission is detected along both PAs, with maximum extension reaching ∼3.2 arcsec (27 kpc) similarly to the east and south of the quasar as shown in Fig. A6. We checked that the emission seen on the trace in the velocity range $-500 < v < 0\,{\rm km\,s^{-1}}$ along PA = NS is real. This emission, however, is barely detected along PA = EW, both because the emission is intrinsically faint and the SNR of the spectrum is lower along this PA. Overall, the spectra of the quasar trace for the two PAs are consistent within the errors (see panel (c) of Fig. A6).

As shown in panel (c) of Fig. A6, the Lyα profile on the quasar trace is clearly asymmetric. Here, the Lyα flux sharply rises on the blue side and slowly decreases on the red side of the profile. Note that the blue edge of the profile (marked by a pink arrow) is close to the systemic redshift of the quasar ($\delta V \sim 60\,{\rm km\,s^{-1}}$). Remarkably, we detect a small peak on the blue side of the profile at $v \sim -300\,{\rm km\,s^{-1}}$. The presence of this peak could be understood in the context of resonant scattering of Lyα photons. Simulations have shown that Lyα radiation should generally escape the galaxy with a double-peaked profile (Verhamme, Schaerer & Maselli 2006; Laursen, Razoumov & Sommer 2009; Noterdaeme et al. 2012) but observations reveal that the blue peak is usually diminished or in some cases completely suppressed (Fynbo et al. 2010). The presence of strong galactic winds, absorption and dust extinction could be responsible for the suppression of the blue peak (Verhamme et al. 2008).

On the other hand, one could also fit a Gaussian function to the Lyα emission seen on the quasar trace. This Gaussian function is shown as a green dotted curve in panel (c) of Fig. A6. One could now reproduce the observed asymmetric Lyα emission profile by putting some Lyα absorption (blue dotted profile in panel (c) of Fig. A6) on top of the green dotted curve. Note that the blue dotted profile, located at $v \sim -40\,{\rm km\,s^{-1}}$ relative to the quasar, is ∼150 km s^{-1} blueshifted with respect to the green dotted curve. This is similar to what is seen in Lyman break galaxies which typically exhibit redshifted emission and blueshifted absorption in Lyα (Shapley et al. 2003). No low-ion is associated with this Lyα absorption while the C IV, Si IV and possibly N V absorption that are seen at $v \sim -635\,{\rm km\,s^{-1}}$ could probably be partly associated with it.

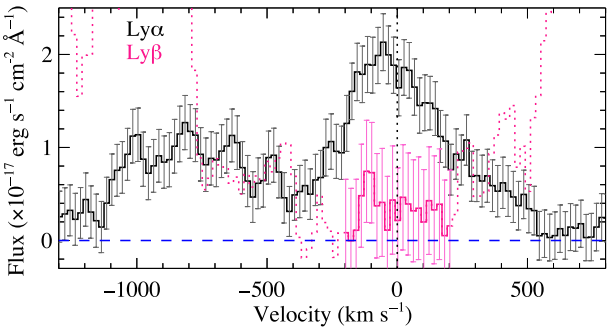

Figure 3. Lyα (black curve) and Ly β (pink curve) emission lines detected in the trough of the damped Lyα and Ly β absorption lines along the line of sight towards the quasar J1253+1007.

3.5 SDSS J125302.00+100742.3

The quasar has the best SNR spectrum in our sample. Unfortunately, the O I λ1304 and He II λ1640 emission lines are not detected and the C III] λ1909 emission line region is heavily affected by sky emission and telluric absorption lines. However, we could still fit Gaussian functions to the C IV and Si IV emission lines to get $z = 3.0150$ and 3.0170, respectively. In the analysis of this system, we adopt $z_{\rm em} = 3.0150$ as the systemic redshift of the quasar. The emission lines and their Gaussian fits are shown in panel (a) of Fig. A7.

Metal absorption lines from O I, C II, C II*, Fe II, Si II, Si II*, Al II, Al III, C IV, and Si IV are detected in the eclipsing DLA along this line of sight (see Fig. A7). A single component fit with $z_{\rm abs} = 3.0312$ and $b = 37.0\,{\rm km\,s^{-1}}$ was conducted on the low-ion species. The redshift and b-value were determined through a simultaneous fit to the five Si II transitions (i.e. Si II λ1190, λ1193, λ1304, λ1526, and λ1808). It can be seen from panel (b) of Fig. A7 that Doppler parameters less than 37 km s^{-1} overpredict the observed Si II λ1808 optical depth. The parameters of the fit to the low and high ion species are reported in Tables 3 and 4. The H I column density of $\log N_{\rm H\,I} = 21.30 \pm 0.10$ was determined by fitting damping profiles on the Lyα and Ly β absorption lines, with the redshift fixed to that of the low-ions (see panel (d) of Fig. A7). By fitting the five detected Si II transitions we derive: [Si/H] $= -1.45 \pm 0.20$. We also tentatively derive [C/H] $= -1.61 \pm 0.20$ and [O/H] > -1.95. From the Fe II λ 1608 absorption we derive [Fe/H] $= -2.53 \pm 0.20$ indicating significant depletion of this element on to dust.

While low-ion absorption profiles are dominated by a single component at $v = 0\,{\rm km\,s^{-1}}$ ($z_{\rm abs} = 3.0312$), high-ion species are mainly seen in three distinct components, namely at $v = 0$, -200, and $-620\,{\rm km\,s^{-1}}$ (see panel (c) of Fig. A7). Out of these three components, N V and O VI are only seen at $v = -620$ and $-200\,{\rm km\,s^{-1}}$, with no N V associated with the DLA at $v = 0\,{\rm km\,s^{-1}}$. Note that N V absorption is the strongest at $v = -620\,{\rm km\,s^{-1}}$; this is also the case for C IV and O VI but not Si IV as it has the weakest absorption at this velocity. This clearly shows that the gas is progressively getting more ionized as we go to higher velocities relative to the DLA. This gas must be located close to the AGN as indicated as well by the presence of Si II* absorption (see Paper I). It is interesting to note that Lyα emission on the trace is detected over a large velocity range (∼1500 km s^{-1}) which covers all these absorption components.

In addition to the narrow Lyα emission line that is detected in the DLA trough, it seems that its corresponding narrow Ly β emission line is also detected in the trough of the damped Ly β absorption profile with the flux ratio of I(Lyα)/I(Ly β) < 9.2, and the integrated flux of $f_{\rm Ly\beta} = (1.8 \pm 0.4) \times 10^{-17}$ erg s^{-1} cm^{-2} (see Fig. 3). This

ratio is for the strongest component of the Lyα emission seen in the range $-400 < v < 400\,\mathrm{km\,s^{-1}}$. For the whole Lyα emission, extending from -1100 to $400\,\mathrm{km\,s^{-1}}$, this ratio is < 14.6. Note that for the temperature range of $100 \leq T_e \leq 20\,000$ this ratio should be in the range $9.5 \leq I(\mathrm{Ly}\alpha)/I(\mathrm{Ly}\,\beta) \leq 4.0$ (Martin 1988). Jiang et al. (2016) also reported the possible detection of Ly β emission in the Ly β absorption trough of a PDLA found towards the quasar SDSS J0952+0114.

As shown in panels (a) and (b) of Fig. A8, the Lyα emission is spatially extended along both PAs. Maximum extension is found to the north reaching out to ∼3.7 arcsec (30 kpc) from the nucleus emission. The velocity spread of the Lyα emission on the quasar trace is $\sim 1560\,\mathrm{km\,s^{-1}}$ which is the largest in our quasar sample (see Table 2 column 8). The kinematic of the extended envelope towards the east and up to a distance of 1.5 arcsec (12 kpc) is remarkably similar to that of the trace (see panel (b) of Fig. A8). The velocity spread of the emission towards the north is $\sim 500\,\mathrm{km\,s^{-1}}$ while it is $\lesssim 300\,\mathrm{km\,s^{-1}}$ to the south and west direction. Note that the spectrum along the east–west direction has a lower SNR because its exposure time is ∼25 per cent shorter than that of the other PA. However, the emission on the quasar trace for the two PAs are still consistent within the errors (see panel (c) of Fig. A8).

The emission on the quasar trace has two main components at $100 \lesssim v \lesssim 800$ and $900 \lesssim v \lesssim 1600\,\mathrm{km\,s^{-1}}$ (see panel (a) of Fig. A8). The velocity difference between the centre of the two components is $\sim 700\,\mathrm{km\,s^{-1}}$. We note that the velocity separation between the DLA and the stronger component of the Lyα emission is $\sim 30\,\mathrm{km\,s^{-1}}$, possibly suggesting they originate in the same region. Note that the velocity separation between the Lyα emission and the quasar itself is not robust as the quasar redshift is derived from the C IV emission line.

4 RESULTS AND DISCUSSION

The Lyα emission seen in the trough of the eclipsing DLAs in our sample are all strong and spatially extended along the two observed PAs. The observed properties of the Lyα emission are summarized in Tables 5 and 6. The values in Table 6 are corrected for the Galactic extinction (using the dust map of Schlegel, Finkbeiner & Davis 1998) and the slit loss effect. The slit loss effect was corrected by assuming that the Lyα nebulae are uniform face-on ellipses with major and minor diameters equal to their extent along the two PAs. We then estimated the amount of flux missed by the slit and consequently corrected the observed luminosities.

4.1 He II emission line

Since it is possible that the extended Lyα emission seen around quasars might arise from the resonant scattering of Lyα photons from the central AGN, observation of other lines with non-resonant characteristic, like He II λ1640, is needed to constrain the importance of this effect. If the observed extension of the Lyα envelope results from resonant scattering, then the corresponding He II emission should not be extended. Similarly, detections of spatially extended He II and Lyα emission on the same scale would imply that resonant scattering of Lyα photons is not important.

The He II λ1640 emission line is detected in the spectra of three of our quasars (i.e. J0112−0048, J1058+0315 and J1154−0215). The spectra of the remaining quasars (i.e. J0823+0529, J0953+0349, and J1253+1007) also show some weak emission features near the expected position of the He II emission line. However, the low SNR of the latter spectra makes the corresponding detections highly uncertain.

We calculated the integrated flux in the expected extended He II emission line region outside the quasar trace as the sum of the flux in all He II pixels of the 2D spectra corresponding to the detected Lyα extended region. The result is listed in the seventh column of Table 5. We calculated the corresponding 3σ detection limit as three times the square root of the sum of the variance of the flux for the same pixels. The result is reported in the eighth column of Table 5. By comparing the values in the seventh and eighth column of Table 5 we can see that no extended He II emission is detected above the 3σ detection limit outside the quasar trace in any of our objects.

We also investigate the possible spatial extension of the He II emission by co-adding and comparing the 2D spectra around the position of the He II λ 1640 and Lyα emission lines (see Fig. 4). Although Lyα emission is very extended off the quasar trace, its corresponding extended He II emission is apparently not detected in the final stacked spectrum. To quantify this, we integrated the 2D spectra along the spatial direction and compared the result to the background noise level. The result is shown as green curves in panels (c) and (d) of Fig. 4 where the 1σ background noise level is marked as horizontal pink dotted lines. Integrating the green curve over the velocity range $-500 \leq v \leq 500$ results in $f_{\mathrm{HeII}} = (1.09 \pm 0.89) \times 10^{-17}\,\mathrm{erg\,s^{-1}\,cm^{-2}}$ which is consistent with no detection.

We also integrated the stacked 2D spectra along the spectral direction and the result is shown as red curves in panels (e) and (f) of Fig. 4. For the He II (resp. Lyα) flux, the integration was performed over the velocity range $-700 < v < +200\,\mathrm{km\,s^{-1}}$ (resp. $-800 < v < +600\,\mathrm{km\,s^{-1}}$). The black curves show the emission in the PSF centred on the trace. The blue curves are the control profiles which are integrated across a wavelength range of the same width as the red lines but ∼100 Å away from the He II and Lyα emission lines centre. The difference between the red and blue curves is shown in panels (g) and (h) of Fig. 4. The profile in panel (g) is consistent with no He II emission detection outside the quasar trace at the limit of our observations.

All this may imply that the extended Lyα emission seen around these quasars has predominantly resonant-scattering origin, or the ratio of the He II/Lyα emission is much smaller than what is usually seen in quasars, radio galaxies and/or Lyα blobs (Lehnert & Becker 1998; Arrigoni Battaia et al. 2015). If one assumes that the expected He II to Lyα flux ratio is ∼0.1 which is the typical value observed in Lyα blobs and radio galaxies (Villar-Martín et al. 2007; Prescott, Dey & Jannuzi 2013; Arrigoni Battaia et al. 2015), then one would expect to detect He II emission at ∼4.5σ towards the two quasars J0112−0048 (along the EW direction) and J0823+0529 (along both PAs). The expected He II emission flux towards the remaining quasars would still be below the 3σ detection limit. The fact that no He II emission is detected above the 3σ detection limit towards J0112−0048 and J0823+0529 suggests that the He II/Lyα ratio towards these two quasars is below 0.1, and thus argues for resonant scattering of Lyα photons being a dominant process in these quasars.

Foltz et al. (1988) and Heckman et al. (1991b) found that the quasar He II emission flux is ∼30 per cent of that of the Lyα envelope while in our case, it is ∼5–10 per cent. The discrepancy could in part be due to the uncertain redshift of the Lyα envelope in Heckman et al. (1991a) narrow band images, which led to ∼30 per cent of uncertainty in their Lyα fluxes. The uncertain redshift of the envelope makes it difficult to precisely place the Lyα emission within the bandpass of an interference filter. Moreover, in Heckman

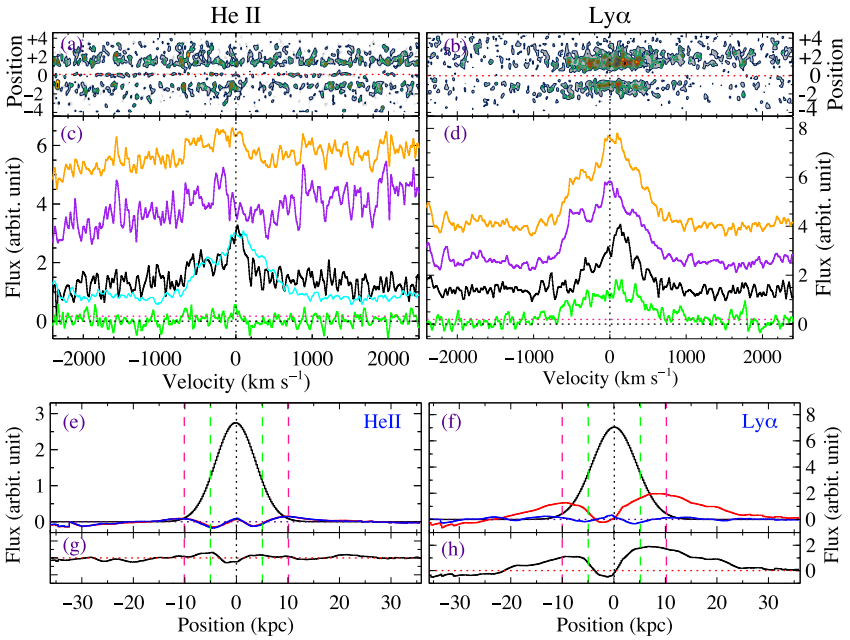

Figure 4. Panels (a) and (b): stacked 2D spectra around the He II and Lyα spectral regions after subtracting the emission on the trace. The red dotted horizontal lines mark the centre of the trace. The y-axis is position in arcsecond. Panels (c) and (d): the green curves show the intensity profiles of the He II and Lyα emission lines integrated over the regions outside the quasar's trace. Actually, the green curves are the 1D profiles of the 2D spectra shown in panels (a) and (b) integrated over the y-axis. The black curves are the stacked 1D spectra of the three quasars (i.e. J0112−0048, J1058+0315, and J1154−0215) for which the He II emission line is detected in the quasar spectrum on the trace. The purple curves are the stacked 1D spectra of the three quasars (i.e. J0823+0529, J0953+0349, and J1253+1007) with uncertain He II detection on the quasar trace. The orange curves are the stacked 1D spectra of all six quasars. For the sake of comparison, the stacked Lyα emission line profile (scaled arbitrarily) is also overplotted as a cyan curve in panel (c). The horizontal pink dotted lines mark the 1σ uncertainty in the flux. The origin of the velocity plots is at $z = 2.5742$ which is the mean redshift of all six quasars. Note that, for the sake of better illustration, the black, purple, and orange profiles are arbitrarily shifted along the y-axis. Panels (e) and (f): the black curve shows the emission in the quasar's PSF centred on the trace, integrated over the spectral width of the He II (resp. Lyα) emission line. The red curve is the intensity profile of the same region but after subtracting the quasar trace and the blue curve is the control profile. The control profile is integrated across a wavelength range of the same width as the red and black curves but centred 100 Å redder (resp. bluer) than the He II (resp. Lyα) emission line. Note that the mean flux of the control region outside the quasar trace was subtracted from the green curve in panel (c) to correct for the non-zero residual flux (see the text). The green and pink vertical dashed lines show the FWHM and full width of the quasar PSF, respectively. Panels (g) and (h): the black curves show the difference between the red and blue curves in panels (e) and (f).

et al. (1991a) sample, in contrast to ours, the Lyα emission from the BLR of the quasar is not extinguished by the presence of a strong eclipsing DLA. Therefore, de-convolution of the strong broad Lyα emission could lead to the underestimation of the Lyα flux of the envelope by oversubtracting the emission close to the central region. In our sample, this effect is minimum.

4.2 Redshift dependence

NC12 suggested that quasars at higher redshifts tend to have fainter envelopes. In Fig. 5, we plot the average surface brightness of the Lyα envelopes as a function of redshift for our sample (black filled circles), together with the CJ06 (red filled stars), NC12 (blue filled squares) and Villar-Martín et al. (2003, pink triangles) objects, all corrected for redshift dimming effect. The envelopes in our sample are $\gtrsim$ 10 times brighter than those at redshift $z \sim 4$. The surface brightness seems to steadily decrease with redshift.

Fig. 6 presents the luminosity of the Lyα envelopes versus redshift. The symbols are the same as in Fig. 5. The luminosity of the Lyα envelopes in our sample are almost the same as those in Villar-Martín et al. (2003) and CJ06. Our brightest envelope has the same total luminosity as the brightest object in NC12 while their faintest object is ∼17 times less luminous than our faintest one.

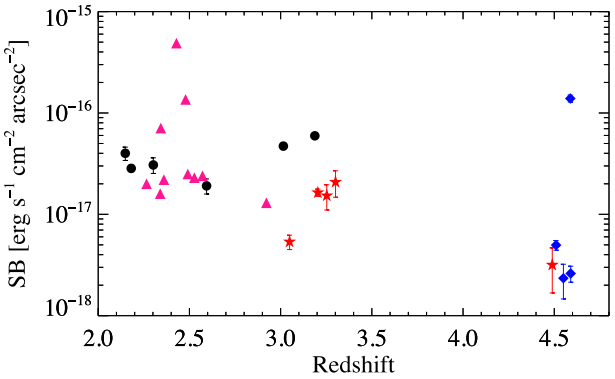

Figure 5. Average surface brightness of the Lyα envelopes as a function of redshift for our sample (black filled circles), together with the CJ06 (red filled stars), NC12 (blue filled squares) and Villar-Martín et al. (2003, pink triangles) objects, all corrected for the redshift dimming effect. The mean redshift of our quasars (i.e. $z \sim 2.5$) is taken as the reference redshift to correct for this effect.

NC12 argued that their lower surface brightness may be due to the deeper sensitivity of their observation which led to the more extended envelopes compared to those of CJ06. The mean size of the envelopes in the NC12, CJ06 and our sample are 45, 26.4 and 41 kpc,

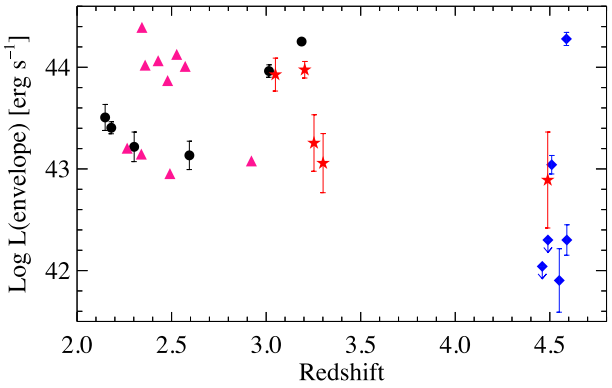

Figure 6. Lyα luminosity of the envelopes versus quasar redshift. The symbols represent the same samples as in Fig. 5.

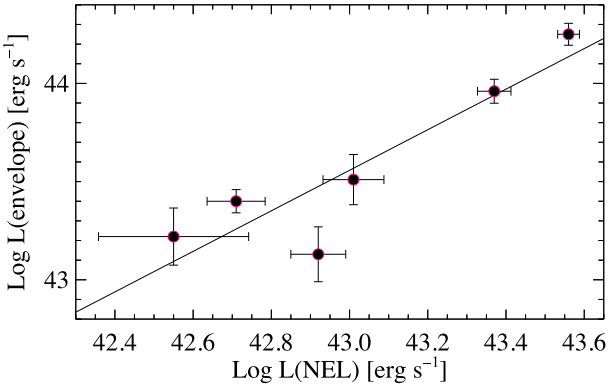

Figure 7. Luminosity of the extended Lyα envelopes versus that of the unresolved NEL for our sample. The black line is the fit to all points.

respectively. The mean detection limit of the NC12 observations is $\sim 2.5 \times 10^{-17}$ erg s^{-1} cm^{-2} (after taking into account the redshift dimming effect) while in our case it is $\sim 4.7 \times 10^{-17}$ erg s^{-1} cm^{-2}. This indicates that the large extent and higher surface brightness of our envelopes cannot be attributed to the depth of the observation. Our envelopes, despite having less depth, still are almost as extended as the NC12's envelopes. This further strengthens the idea put forth by NC12 that higher redshift envelopes may intrinsically be fainter than their lower redshift descendants.

We also checked for any correlation between the surface brightness of the envelope and the velocity width of the Lyα emission line in our sample, and found a mild correlation between them. The correlation coefficient is 0.64 implying a 17 per cent probability of finding this trend by chance occurrence. If we take into account the NC12 and CJ06 samples, then the correlation disappears, suggesting that the trend found in our sample may not be real. However, the number of quasars is not large enough to be statistically significant. Observation of a large sample of quasars with extended Lyα envelope may help us settle this question.

4.3 Quasar narrow Lyα emission

If the narrow Lyα emission on the spectrum trace is associated with the unresolved inner part of the extended Lyα envelope as suggested by Heckman et al. (1991b) then one would expect a correlation between the Lyα luminosity on the trace and in the extended region. Since the narrow Lyα emission line in a quasar spectrum is usually strongly blended and contaminated by the emission from the BLR, no attempt has ever been made to correlate its luminosity with that of the extended envelope. For the first time, in this work we can directly examine this correlation for the objects in our sample. Fig. 7 presents the luminosity of the extended Lyα envelopes as a function of the luminosity of the Lyα emission seen on the quasar trace for the objects in our sample. A strong correlation with a coefficient of 0.90 is found between the two luminosities. This correlation implies that much of the narrow spatially unresolved Lyα emission seen on the quasar trace is probably associated with the inner part of the extended Lyα envelope. This correlation can be interpreted as a consequence of the direct influence of the quasars on their Lyα envelopes.

4.4 Quasar versus the envelope luminosities

We investigate the possible correlation between the broad Lyα line luminosity of the quasars and that of the extended Lyα envelopes.

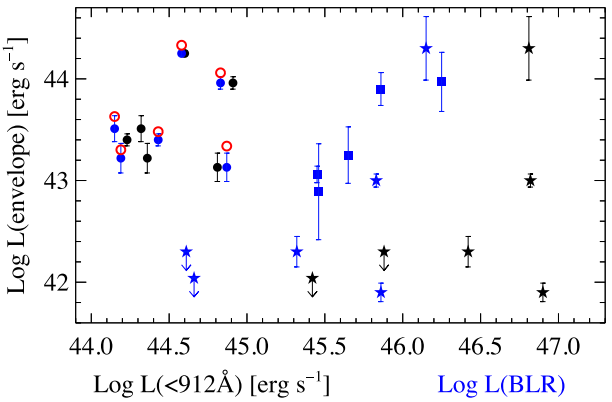

Figure 8. Luminosity of the Lyα envelope versus that of the Lyα BLR (blue symbols) and quasar ionizing radiation (black symbols) for the NC12 (stars), CJ06 (squares) and our sample (filled circles). The red circles show the total observed Lyα luminosity as a function of that of the expected Lyα BLR in our sample.

Since the broad Lyα emission line is fully extinguished in our spectra, its luminosity is calculated from the principle component analysis (PCA) reconstruction of this line (Pâris et al. 2011, 2014). To be consistent with previous work, we integrate the 1D quasar spectra in the rest-frame wavelength interval of 1200–1230 Å and then measure the luminosity. The result is shown in Fig. 8 as blue symbols. The correlation coefficient for the data points in the CJ06 (blue squares), NC12 (blue stars), our quasars (blue filled circles) and for the combination of the three samples are 0.92, 0.61, 0.24 and 0.11, respectively. The lack of a correlation in the combined sample mainly stems from the absence of a correlation in our sample. We added the luminosity of the unresolved NEL to that of the extended envelope in our sample (the result is shown as red open circles in Fig. 8), and still found no correlation with the Lyα BLR luminosity.

We also investigated whether the extended Lyα envelope luminosities are correlated with the ionizing radiation flux from the quasars. We used the same technique described in Paper I to estimate the ionizing flux of the quasars in our sample. The result is shown as black symbols in Fig. 8. We found correlation coefficients of 0.20, 0.32 and −0.41 for the objects in the NC12, our sample and the total sample, respectively. The lack of a strong correlation between the quasar luminosity and that of its envelope may suggest that processes other than direct photoionization are at play such as variations of covering factors and/or dust extinction from one line of sight to the other.

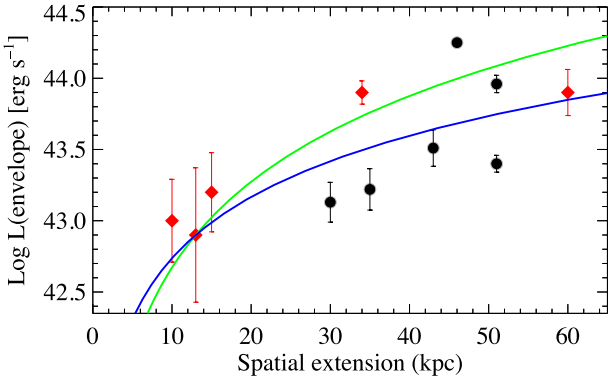

Figure 9. Luminosity of the Lyα envelopes as a function of their spatial extension for the CJ06 (red squares) and our sample (black filled circles). The green and blue curves show power-law functions with index $\alpha = 0.5$ and 0.7, respectively (see the text).

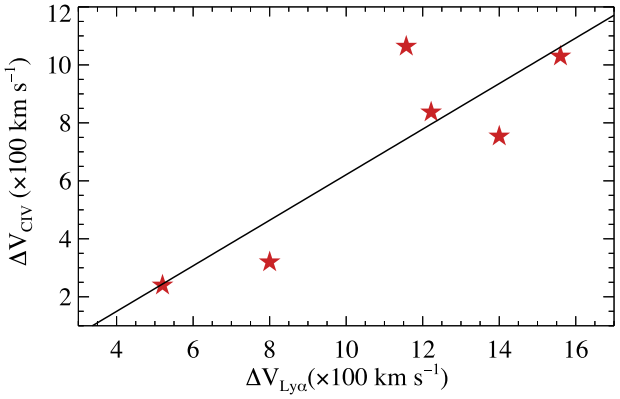

Figure 10. Relation between the velocity extent of the Lyα emission and that of the C IV absorption profile in our sample. The black line is a fit to all data points.

4.5 Spatial and velocity extent of the nebulae

The mean sizes (i.e. diameter) of the envelopes in the NC12, CJ06 and our sample are 45, 26 and 41 kpc, respectively. The depth of the observation in our sample is very similar to that of the CJ06 while the NC12 observations are the deepest. This suggests that our envelopes could be more extended if our observations were as deep as the NC12 ones.

The Lyα envelopes around our quasars exhibit two-sided emissions along both PAs. This is in contrast to the CJ06 sample of RQQs in which only one-sided emission is detected. Although one-sided and two-sided envelopes are both reported around RQQs (e.g. Møller et al. 2000; Weidinger et al. 2005), RLQs are usually observed to have asymmetric two-sided nebulae (Heckman et al. 1991a). Our envelopes, therefore, seem to morphologically resemble those found around RLQs. Fig. 9 presents the luminosity of the Lyα envelopes as a function of their spatial extension for the CJ06 (red diamonds) and our sample (black filled circles). A strong correlation with a high probability of ∼99.6 per cent is found between the Lyα luminosity of the extended envelope and its spatial extension for the full sample. This strong correlation confirms the result by CJ06 that more luminous envelopes are also spatially more extended.

Kaspi et al. (2000, 2005) found a relation between the luminosity of the AGN and the size of the BLR, $R_{BLR} \sim L^{\alpha}$ (also see Bentz et al. 2013). Their best value of α is in the range $0.5 < \alpha < 0.7$ which is consistent with simple photoionization expectations. Interestingly, similar relation seems to be present between the size of the extended Lyα envelope and its luminosity. In Fig. 9, the green and blue curves show the power-law functions for $\alpha = 0.5$ and 0.7, respectively. This could imply that the Lyα envelopes may be strongly affected by the ionizing radiation emanating from the central AGN. The scatter seen in our observed data points around this mean power-law relation may result from the non-uniform conditions in the emission regions. Part of this scatter could also be due to the presence of dust in these regions.

In Paper I, we suggested that the high ionization gas seen towards J0823+0529 may arise from some warm absorber driven by the accretion disc luminosity. The outflowing material is then stopped by collision with the ISM of the host galaxy, producing shock waves. The shocked material then gets cooled and mixed with the ISM. The outflowing material could also affect the kinematics of the ISM gas. If true, then one would expect a correlation between the kinematics of the ISM gas and that of the outflowing material. In Fig. 10, we plot the relation between the total velocity extension of the Lyα emission and that of the C IV absorption profile reported in Table 2. A correlation coefficient of 0.86 is found in this sample. This correlation may hint at the possibility that the Lyα emission envelopes around the quasars in our sample may be affected by the outflowing material originated from the innermost region of the AGN. However, observation of more quasars with extended Lyα emission are needed to confirm whether this correlation is real.

4.6 Physical properties of the eclipsing DLAs

The first systematic study of the physical properties of PDLAs was done by Ellison et al. (2010, hereafter EP10; also see Ellison et al. 2002). They studied in detail, a sample of 16 PDLAs with a velocity separation $\delta V < 3000\,km\,s^{-1}$ from the quasars. They compared the properties of their PDLAs with those of a control sample of intervening DLAs to investigate the differences between the two populations. Their control sample contains intervening DLAs with $\delta V > 10\,000\,km\,s^{-1}$ from the Berg et al. (2015 b) catalog. In this section, we compare our DLAs with those of EP10 and the control sample.

The velocity offset between the quasars and the eclipsing DLAs in our sample is in the range $-809 \lesssim \delta V \lesssim 1207\,km\,s^{-1}$ (see Table 2 column 5). 5 out of 6 DLAs have positive velocity offset (i.e. DLAs falling towards the quasars) while in the EP10 sample it is 4 out of 16. It is interesting to note that the only object with a negative velocity offset in our sample (i.e. J1058+0315) has also the smallest Lyα velocity extent ($\Delta V_{Ly\alpha} \sim 520\,km\,s^{-1}$) and the simplest C IV absorption feature with only one single component. Moreover, the maximum velocity offset of ∼882 km s^{-1} between the DLA and the extended Lyα emission in our sample is also seen along this line of sight.

4.6.1 *Ionization properties*

In our eclipsing DLAs we detect high ionization species which in many cases extend hundreds of km s^{-1} to the blue of the main low-ion component. C IV and Si IV absorption are detected in all of our eclipsing DLAs. The O VI region in most of our spectra suffers from low SNR and contamination with Lyα forest absorption. None the less, the O VI doublet is detected in the relatively high SNR spectrum of the quasar J1253+1007 in the velocity range $-850 \lesssim \delta V \lesssim -100\,km\,s^{-1}$ (see Fig. A7). Although the O VI λ1037

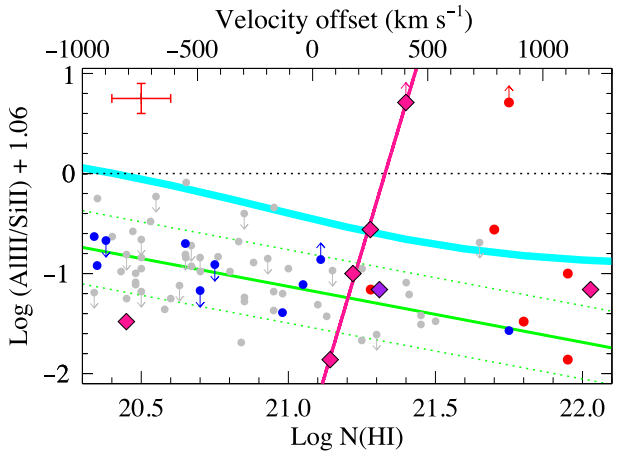

Figure 11. The Al III/Si II ratio as a function of N(H I) for the Berg et al. (2015, grey points), EP10 (blue points), and our eclipsing DLAs (red points). The red error bar on the upper left side of the plot shows the uncertainty in the column densities of our data points. The green solid line is the fit to the Berg et al. (2015) DLAs. The two green dotted lines show the standard deviation of the grey points. The thick cyan line shows the result of a grid of CLOUDY models constructed for the ionization parameter log U = 0.0, a nominal hydrogen density log $n_{H\,I}$ = 1.0, and hydrogen column density in the range $20.30 \leq \log N(\mathrm{H\,I}) \leq 22.10$. The pink diamonds show the Al III/Si II ratios in our sample as a function of the velocity offset between the DLAs and their background quasars (upper x-axis scale where positive values indicate a redshift i.e. the DLAs falling towards the quasars). The pink line shows the fit to the data points with positive velocity offsets, after excluding the point at log N(H I) < 21.5 corresponding to J1253+1007. The purple diamond shows the value for the DLA towards J1253+1007, after correcting the quasar redshift for systemic shift (see the text).

absorption seems to be slightly blended with some Lyα forest absorption, the similarity between the O VI λ 1031 and the N V doublet absorption confirms the detection. At zero velocity, we have one detection (towards J0823+0529) and one strict upper limit (towards J1253+1007) of N V, with no confident N V detection towards the remaining objects. Offset N V and Si IV absorption are seen to the blue at $v \lesssim -100\,\mathrm{km\,s^{-1}}$ towards J0953+0349, J1154−0215, and J1253+1007. Moreover, offset C IV absorption is also seen at $v \lesssim -100\,\mathrm{km\,s^{-1}}$ towards all our objects except J1058+0315. EP10 found no low-ions associated with their offset high ions while in our case, some strong low-ion transitions (e.g. O I, C II, C II*) are seen towards J0953+0349 at $v \sim -660\,\mathrm{km\,s^{-1}}$.

In J0953+0349, the velocity separation between the quasar and the two low-ion components are −484 and 175 km s^{-1} (see panel (a) in Fig. A1). This is reminiscent of the PDLA studied by Rix et al. (2007) towards the quasar Q2343−BX415. They found two low-ion components, one redshifted by ∼400 km s^{-1} and the other blueshifted by ∼170 km s^{-1} relative to the quasar systemic redshift (see their fig. 5). They concluded that the presence of prominent high ionization lines in the redshifted component along with the partial coverage of the continuum source (Ofengeim et al. 2015; Klimenko et al. 2015) are indicative of gas falling on to the central AGN; and the blueshifted component may be part of the outflowing material of the quasar host galaxy.

The column density ratio N(Al III)/N(Al II) can be used to study the ionization properties of DLAs. Vladilo et al. (2001) showed that, in the presence of a soft stellar-type ionizing radiation, this ratio decreases when N(H I) increases. Fig. 11 shows Al III/Si II ratios (after correcting for the solar value of Al/Si) as a function of N(H I) for the Berg et al. (2015, grey points), EP10 (blue points), and our DLAs (red points). In this figure, Si II is used as a proxy for Al II which is mostly saturated in DLAs. EP10 found no apparent difference between the intervening DLAs and their PDLAs. In Fig. 11, the green solid line, which clearly shows the anti-correlation with N(H I), is the fit to the Berg et al. (2015) DLAs. The two green dotted lines mark the 1σ uncertainty in the Al III/Si II ratios, calculated from the standard deviation of the grey data points in Fig. 11. Interestingly, three of our eclipsing DLAs seem to follow this anti-correlation, implying that the DLA gas is photoionized by a soft radiation and/or if it is close to the AGN, the ionization parameter is very low (Howk & Sembach 1999). The remaining three eclipsing DLAs indicate rather elevated Al III/Si II ratios, with one DLA (towards J1154−0215) having the highest Al III/Si II ratio ($\gtrsim$+0.71) ever reported for a DLA or PDLA.

In Fig. 11, the thick cyan line shows the result of a grid of CLOUDY models constructed for the ionization parameter log U = 0.0 and a nominal hydrogen density log $n_{H\,I}$ = 1.0. The combination of the mean AGN spectrum of Mathews & Ferland (1987), the cosmic microwave background (CMB) radiation at z = 2.5742 (mean redshift of all our eclipsing DLAs), and the Haardt-Madau extragalactic spectrum (Haardt & Madau 1996) at the same redshift is taken as the incident radiation hitting the cloud. Note that the mean metallicity <[Si/H]> = −1.2 is assumed although the result is not very sensitive to the choice of the metallicity and redshift. As shown in Fig. 11, two of our eclipsing DLAs seem to have Al III/Si II ratios consistent with this CLOUDY model.

As mentioned above, the Al III/Si II ratio in the eclipsing DLA towards J1154−0215 is $\gtrsim$+0.71 which is ∼6 times more than the highest value in the Berg et al. (2015) DLA sample (see Fig. 11). We note that this value can even be considered as a *strict* lower limit because the Si II (resp. Al III) column density can be considered as a *strict* upper limit (resp. lower limit; see below and Fig. A5). To get the Si II column density, a Voigt profile fit was conducted on the Si II λ 1808 and λ 1526 absorption lines. Since the former transition is weak and the latter one is slightly blended to the red, the derived N(Si II) is taken as an upper limit. On the other hand, the Al III absorption profiles are most probably saturated as the two components seem to have almost the same optical depth. The high value of Al III/Si II ratio towards J1154−0215 could be explained if one assumes a two- or multi-phase medium.

In Fig. 11, the pink diamonds show the Al III/Si II ratios in our sample as a function of the velocity offset between the DLAs and their quasars. In this figure, the upper x-axis represents the velocity offsets in km s^{-1}, and positive values indicate a redshift (i.e. the DLAs falling towards the quasar). Taken at face value, there appears to be a strong correlation (with the coefficient of 0.99) between the velocity offsets and the Al III/Si II ratios among the DLAs with positive velocity offset. The only exception to this is the DLA towards J1253+1007 which exhibits a high positive velocity offset of ∼1207 km s^{-1}, and apparently does not follow this trend. We note that the redshift of this quasar was obtained by fitting its C IV emission line (see Fig. A7). So, if we apply the known systematic shift of C IV emission line (as reported in Shen et al. 2007) to correct the redshift, we get a velocity offset of ∼290 km s^{-1} (instead of ∼1207 km s^{-1}) between the DLA and the quasar. This new value, which is now more consistent with the correlation mentioned above, is shown as a purple square in Fig. 11. Note that the pink line shows the fit to the data points of DLAs with positive velocity offset, after excluding the one towards J1253+1007. It could be possible that eclipsing DLAs with positive velocity offset are

chemically distinct from those with negative velocity offset. The DLA towards J1058+0315 with negative velocity offset of $-809\,\mathrm{km\,s^{-1}}$ is probably an intervening gas.

This correlation strongly suggests that DLAs with higher velocity towards the quasars have also higher ionization and therefore may be closer to the AGN which is consistent with the fact that they could be part of an infall flow on to the host galaxy.

4.6.2 The size of the eclipsing DLAs

Since extended Lyα emission is detected in the trough of our eclipsing DLAs, this indicates that the size of the absorbing cloud should be smaller than that of the Lyα emitting central unresolved region. In Paper I, we studied in detail the eclipsing DLA seen towards the quasar J0823+0529, which also exhibits some indications of partial coverage of the BELR. We used the CLOUDY photoionization code to model the absorber including the Si II* absorption and derived hydrogen density in the range $180 < n_{\rm H} < 710\ \mathrm{cm^{-3}}$, resulting in the cloud size in the range $2.3 < l(\mathrm{H\,I}) < 9.1$ pc.

Si II* absorption is also detected in the eclipsing DLA towards quasar J1253+1007 (see Fig. A7). Following the same approach as in Paper I, we get $n_{\rm H} \sim 13\ \mathrm{cm^{-3}}$ and $l(\mathrm{H\,I}) \sim 50$ pc. Unfortunately, in the other 4 objects in our sample, the Si II* absorption is not detected.

Assuming, as in e.g. Prochaska & Hennawi (2009) that the optically thick eclipsing DLAs in our sample have $n_{\rm H} > 10\ \mathrm{cm^{-3}}$, we can derive an indicative upper limit on their size (i.e. $l \sim N_{\rm H\,I}/n_{\rm H}$). The result is given in the last column of Table 2 where the values are in pc. As shown in this table, all our eclipsing DLAs appear to have sizes smaller than 300 pc. Since NELRs in quasars have dimensions of several hundreds of parsecs, our upper limits on the size of the eclipsing DLAs are consistent with the argument that the clouds are smaller than the central unresolved emission region.

5 SUMMARY AND CONCLUSIONS

We present spectroscopic observations of six high redshift ($z_{\rm em} > 2$) quasars, which have been selected because of the presence of a strong proximate ($z_{\rm abs} \sim z_{\rm em}$) coronagraphic DLA which covers only the broad line region of the quasar, thus revealing emission from the host galaxy. We detect spatially extended Lyα emission envelopes around the six quasars, with projected spatial extent in the range $26 \leq d_{\mathrm{Ly}\,\alpha} \leq 51$ kpc. No correlation is found between the quasar ionizing luminosity and the Lyα luminosity of their extended envelopes. This could be related to the limited covering factor of the extended gas and/or due to the AGN being obscured in other directions than towards the observer. Indeed, we find a strong correlation between the luminosity of the envelope and its spatial extent, which suggests that the envelopes are probably ionized by the AGN. The metallicity of the coronagraphic DLAs is low and varies in the range $-1.75 < [\mathrm{Si/H}] < -0.63$. Highly ionized gas is observed associated with most of these DLAs, probably indicating ionization by the central AGN. One of these DLAs has the highest Al III/Si II ratio ever reported for any intervening and/or proximate DLA. Most of these DLAs are redshifted with respect to the quasar, implying that they might represent infalling gas probably accreted on to the quasar host galaxies through filaments.

5.1 Nature of the emitting gas

The main mechanisms proposed to power the extended Lyα emission envelopes around high redshift quasars are photoionization by the AGN, and cold accretion of neutral hydrogen gas into the quasar dark matter halo. If ionizing photons from the AGN are responsible for powering the extended Lyα emission, a correlation between the quasar and its envelope luminosities is expected. On the other hand, in the cold accretion scenario, no such correlation is expected.

CJ06 found no correlation between the quasar ionizing luminosity and the luminosity of the Lyα envelope. They argued that the lack of correlation cannot be due to extinction by dust or absorption by neutral hydrogen in the quasar environments which could potentially affect the quasar luminosity at 912 Å. Similarly, NC12 found no correlation between the two luminosities for their full sample, apparently confirming the CJ06 result, but at higher redshifts and for a larger luminosity range. NC12 argued that removing the object BR 2237−0607 from their sample would restore the correlation, implying that the quasar might be the main powering source of the Lyα envelope. But the lack of a correlation for their full sample seems to favour the cold accretion scenario.

In our sample, the quasar ionizing luminosity does not seem to correlate with the extended Lyα envelope luminosity. This is consistent with what is seen in CJ06 and NC12 full samples. However, in Section 4.5, we found a strong correlation between the luminosity of the Lyα envelope and its spatial extension. We suggested that this correlation could imply that the quasar ionizing flux might be powering the Lyα envelopes. This seems to be at odds with the apparent lack of a correlation between the quasar ionizing luminosity and the Lyα envelope luminosity. It is possible that the level of extinction by dust significantly varies from one object to the other in our sample, resulting in highly uncertain measurement of the intrinsic quasar luminosities at 912 Å. Moreover, in contrast to the CJ06 and NC12 samples, the presence of the strong eclipsing DLAs at the quasar emission redshift in our sample would also mean higher absorption of the quasar flux by the surrounding neutral hydrogen. These effects could in principle remove the possible correlation that might have existed between the luminosity of the quasar at 912 Å and that of the Lyα envelope in our sample. To circumvent this problem, one can use the infrared spectra of the quasars to better calibrate the quasar template spectrum and consequently get a better estimate of the quasar luminosity at 912 Å. Better estimate of the quasars ionizing luminosities might restore the correlation.

5.2 Nature of the eclipsing DLAs

An important question regarding the origin of the proximate DLAs is whether they are due to outflowing material intrinsic to the quasar or some (infalling) material unrelated to the AGN environment but coincident in redshift with the background quasar. If the DLA is part of some low density ($n_{\rm H} < 10\ \mathrm{cm^{-3}}$) infalling material close to the central AGN, the quasar's ionizing photons could ionize and photoevaporate it (Prochaska & Hennawi 2009). Although infalling gas is usually expected to have lower metallicity, associated outflowing absorbers tend to have solar or super solar metallicities (Petitjean, Rauch & Carswell 1994). This would in principle allow one to distinguish whether the gas is associated or intervening.

EP10 found that their PDLAs with higher H I column densities have metallicities ∼3 times higher than what is seen for the intervening DLAs, but still below those expected for an associated absorber. They argued that their PDLAs are probably neither associated nor intervening. They suggested that PDLAs probably probe overdense regions in massive galaxies with higher metallicities in dense clusters.

The metallicities of our eclipsing DLAs are low and similar to what is seen in intervening DLAs. This would imply that these

absorbers might not be outflowing material driven by the central AGN. The fact that most of our eclipsing DLAs have redshifts larger than that of their background quasars further strengthens the idea that these DLAs could be associated with some less enriched infalling material accreting on to the quasar host galaxies, probably through filaments as was concluded for the quasar J0823+0529 (Fathivavsari et al. 2015).

ACKNOWLEDGEMENTS

This article is based on data obtained with MagE at the Clay telescope of the Las Campanas Observatory (CNTAC Prgm. ID CN2012B-51 and CN2013A-121) and with XSHOOTER at the ESO/VLT in Chile as a part of ESO programme 091.A-0299(A). We would like to thank the anonymous referee for his/her constructive comments, which helped us to improve the paper. We also thank George Becker for advices on MagE data reduction and Hadi Rahmani for useful discussion. HFV was supported by the Agence Nationale pour la Recherche under programme ANR-10-BLAN-0510-01-02. SL has been supported by FONDECYT grant number 1140838 and partially by PFB-06 CATA.

REFERENCES

Adelberger K. L., Shapley A. E., Steidel C. C., Pettini M., Erb D. K., Reddy N. A., 2005, ApJ, 629, 636
Arrigoni Battaia F., Yang Y., Hennawi J. F., Prochaska J. X., Matsuda Y., Yamada T., Hayashino T., 2015, ApJ, 804, 26
Arrigoni Battaia F., Hennawi J. F., Cantalupo S., Prochaska J. X., 2016, preprint (arXiv:1604.02942)
Asplund M., Grevesse N., Sauval A. J., Scott P., 2009, ARA&A, 47, 481
Bahcall J. N., Spitzer L. J., 1969, ApJ, 156, 63
Bentz M. C. et al., 2013, ApJ, 767, 149
Berg T. A. M., Ellison S. L., Prochaska J. X., Venn K. A., Dessauges-Zavadsky M., 2015, MNRAS, 452, 4326
Bergeron J., Petitjean P., Cristiani S., Arnouts S., Bresolin F., Fasano G., 1999, A&A, 343, 40
Bergeron J. et al., 2004, The Messenger, 118, 40
Bordoloi R., Rigby J. R., Tumlinson J., Bayliss M. B., Sharon K., Gladders M. G., Wuyts E., 2016, MNRAS, 458, 1891
Borisova E., Cantalupo S., Lilly S. J., Marino R. A., Gallego S. G., Bacon R., Blaizot J., Bouché N., 2016, preprint (arXiv:1605.01422)
Bouché N., Murphy M. T., Péroux C., Davies R., Eisenhauer F., Förster Schreiber N. M., Tacconi L., 2007, ApJ, 669, 5
Bunker A., Smit J., Spinrad H., Stern D., Warren S., 2003, Ap&SS, 284, 357
Cantalupo S., Arrigoni-Battaia F., Prochaska J. X., Hennawi J. F., Madau P., 2014, Nature, 506, 63
Christensen L., Jahnke K., Wisotzki L., Sánchez S. F., 2006, A&A, 459, 717 (CJ06)
Churchill C. W., Trujillo-Gomez S., Nielsen N. M., Kacprzak G. G., 2013, ApJ, 779, 87
Courbin F., North P., Eigenbrod A., Chelouche D., 2008, A&A, 488, 91
Croft R. A. C., Hernquist L., Springel V., Westover M., White M., 2002, ApJ, 580, 634
D'Odorico V., Petitjean P., Cristiani S., 2002, A&A, 390, 13
D'Odorico V. et al., 2013, MNRAS, 435, 1198
Dawson K. S. et al., 2013, AJ, 145, 10
Dijkstra M., Loeb A., 2009, MNRAS, 400, 1109
Ellison S. L., Yan L., Hook I. M., Pettini M., Wall J. V., Shaver P., 2002, A&A, 383, 91
Ellison S. L., Prochaska J. X., Hennawi J., Lopez S., Usher C. Wolfe A. M., Russell D. M., Benn C. R., 2010, MNRAS, 406, 1435 (EP10)
Erb D. K., Steidel C. C., Shapley A. E., Pettini M., Reddy N. A., Adelberger K. L., 2006, ApJ, 647, 128
Fardal M. A., Katz N., Gardner J. P., Hernquist L., Weinberg D. H., Davé R., 2001, ApJ, 562, 605
Fathivavsari H., Petitjean P., Ledoux C., Noterdaeme P., Srianand R., Rahmani H., Ajabshirizadeh A., 2013, MNRAS, 435, 1727
Fathivavsari H., Petitjean P., Noterdaeme P., Pâris I., Finley H., López S., Srianand R., Sánchez P., 2015, MNRAS, 454, 876 (Paper I)
Finley H. et al., 2013, A&A, 558, 111
Foltz C. B., Chaffee F. H., Jr, Weyman R. J., Anderson S. F., 1988, in Blades J. C., Turnshek D. A., Norman C. A., eds, Proc. QSO Absorption Line Meeting, QSO Absorption lines: Probing the Universe. Cambridge Univ. Press, Cambridge, p. 53
Fried J. W., 1998, A&A, 331, 73
Fynbo J. U., Burud I., Møller P., 2000, A&A, 358, 88
Fynbo J. P. U. et al., 2010, MNRAS, 408, 2128
Haiman Z., Rees M. J., 2001, ApJ, 556, 87
Haiman Z., Spaans M., Quataert E., 2000, ApJ, 537, 5
Haardt F., Madau P., 1996, ApJ, 461, 20
Heckman T. M., Miley G. K., Lehnert M. D., van Breugel W., 1991a, ApJ, 370, 78
Heckman T. M., Lehnert M. D., Miley G. K., van Breugel W., 1991b, ApJ, 381, 373
Hennawi J. F., Prochaska J. X., 2007, ApJ, 655, 735
Hennawi J. F. et al., 2006, ApJ, 651, 61
Hennawi J. F., Prochaska J. X., Kollmeier J., Zheng Z., 2009, ApJ, 693, 49
Hennawi J. F., Prochaska J. X., Cantalupo S., Arrigoni-Battaia F., 2015, Science, 348, 779
Howk J. C., Sembach K. R., 1999, ApJ, 523, 141
Hu E. M., Cowie L. L., 1987, ApJ, 317, 7
Jiang P., Zhou H., Pan X., Jiang N., Shu X., Wang H., Gu Q., Li Z., 2016, ApJ, 821, 1
Kaspi S., Smith P. S., Netzer H., Maoz D., Jannuzi B. T., Giveon U., 2000, ApJ, 533, 631
Kaspi S., Maoz D., Netzer H., Peterson B. M., Vestergaard M., Jannuzi B. T., 2005, ApJ, 629, 61
Kelson D. D., 2003, PASP, 115, 688
Kennicutt R. C., Jr, 1998, ARA&A, 36, 189
Klimenko V. V., Balashev S. A., Ivanchik A. V., Ledoux C., Noterdaeme P., Petitjean P., Srianand R., Varshalovich D. A., 2015, MNRAS, 448, 280
Komatsu E. et al., 2011, ApJS, 192, 18
Landoni M., Falomo R., Treves A., Scarpa R., Farina E. P., 2016, MNRAS, 457, 267
Laursen P., Razoumov A. O., Sommer-Larsen J., 2009, ApJ, 696, 853
Lehnert M. D., Becker R. H., 1998, A&A, 332, 514
Maiolino R. et al., 2012, MNRAS, 425, 66
Marshall J. L. et al., 2008, in McLean I. S., Casali M. M., eds, Proc. SPIE Vol. 7014, Ground-based and Airborne Instrumentation for Astronomy II. SPIE, Bellingham, p. 701454
Martin P. G., 1988, ApJS, 66, 125
Martin D. C., Chang D., Matuszewski M., Morrissey P., Rahman S., Moore A., Steidel C. C., Matsuda Y., 2014, ApJ, 786, 107
Mathews W. G., Ferland G. J., 1987, ApJ, 323, 456
Møller P., Warren S. J., Fall S. M., Jakobsen P., Fynbo J. U., 2000, The Messenger, 99, 31
North P. L., Courbin F., Eigenbrod A., Chelouche D., 2012, A&A, 542, 91 (NC12)
Noterdaeme P., Laursen P., Petitjean P., Vergani S. D., Maureira M. J., Ledoux C., Fynbo J. P. U., López S., Srianand R., 2012, A&A, 540, 63
Ofengeim D. D., Balashev S. A., Ivanchik A. V., Kaminker A. D., Klimenko V. V., 2015, Ap&SS, 359, 26
Pâris I. et al., 2011, A&A, 530, 50
Pâris I. et al., 2014, A&A, 563, 54
Péroux C. et al., 2016, MNRAS, 457, 903
Petitjean P., Vergani S. D., 2011, C. R. Phys., 12, 288
Petitjean P., Rauch M., Carswell R. F., 1994, A&A, 291, 29
Petitjean P., Theodore B., Smette A., Lespine Y., 1996a, A&A, 313, 25
Petitjean P., Pécontal E., Valls-Gabaud D., Charlot S., 1996b, Nature, 380, 411
Prescott M. K. M., Dey A., Jannuzi B. T., 2013, ApJ, 762, 38

Prochaska J. X., Hennawi J. F., 2009, ApJ, 690, 1558
Quiret S., Péroux C., Zafar T., Kulkarni V. P., Jenkins E. B., Milliard B., Rahmani H., Popping A., 2016, MNRAS, 458, 4074
Rix S. A., Pettini M., Steidel C. C., Reddy N. A., Adelberger K. L., Erb D. K., Shapley A. E., 2007, ApJ, 670, 15
Rubin K. H. R., Prochaska J. X., Koo D. C., Phillips A. C., 2012, ApJ, 747, 26
Ryan-Weber E. V., Pettini M., Madau P., Zych B. J., 2009, MNRAS, 395, 1476
Schlegel D. J., Finkbeiner D. P., Davis M., 1998, ApJ, 500, 525
Shen Y. et al., 2007, AJ, 133, 2222
Shapley A. E., Steidel C. C., Pettini M., Adelberger K. L., 2003, ApJ, 588, 65
Shull J. M., Danforth C. W., Tilton E. M., 2014, ApJ, 796, 49
Shull J. M., Moloney J., Danforth C. W., Tilton E. M., 2015, ApJ, 811, 3
Silk J., Rees M. J., 1998, A&A, 331, 1
Simcoe R. A., Sargent W. L. W., Rauch M., 2004, ApJ, 606, 92
Srianand R., Hussain T., Noterdaeme P., Petitjean P., Krühler T., Japelj J., Pâris I., Kashikawa N., 2016, MNRAS, 460, 634
Steidel C. C., Sargent W. L. W., Dickinson M., 1991, AJ, 101, 1187
Steidel C. C., Adelberger K. L., Shapley A. E., Pettini M., Dickinson M., Giavalisco M., 2000, ApJ, 532, 170
Steidel C. C., Erb D. K., Shapley A. E., Pettini M., Reddy N., Bogosavljevic M., Rudie G. C., Rakic O., 2010, ApJ, 717, 289
Swinbank A. M. et al., 2015, MNRAS, 449, 1298
Verhamme A., Schaerer D., Maselli A., 2006, A&A, 460, 397
Verhamme A., Schaerer D., Atek H., Tapken C., 2008, A&A, 491, 89
Vernet J. et al., 2011, A&A, 536, 105
Villar-Martín M., Humphrey A., De Breuck C., Fosbury R., Binette L., Vernet J., 2007, MNRAS, 375, 1299
Villar-Martín M., Vernet J., di Serego Alighieri S., Fosbury R., Humphrey A., Pentericci L., 2003, MNRAS, 346, 273
Vladilo G., Centurión M., Bonifacio P., Howk J. C., 2001, ApJ, 557, 1007
Weidinger M., Møller P., Fynbo J. P. U., 2004, Nature, 430, 999
Weidinger M., Møller P., Fynbo J. P. U., Thomsen B., 2005, A&A, 436, 825
Yang Y., Zabludoff A. I., Davé R., Eisenstein D. J., Pinto P. A., Katz N., Weinberg D. H., Barton E. J., 2006, ApJ, 640, 539

APPENDIX A

Figs A1 to A8 show the 1D and 2D emission spectra along with the fits to the absorption lines for the quasars J0953+0349, J1058+0315, J1154-0215 and J1253+1007.

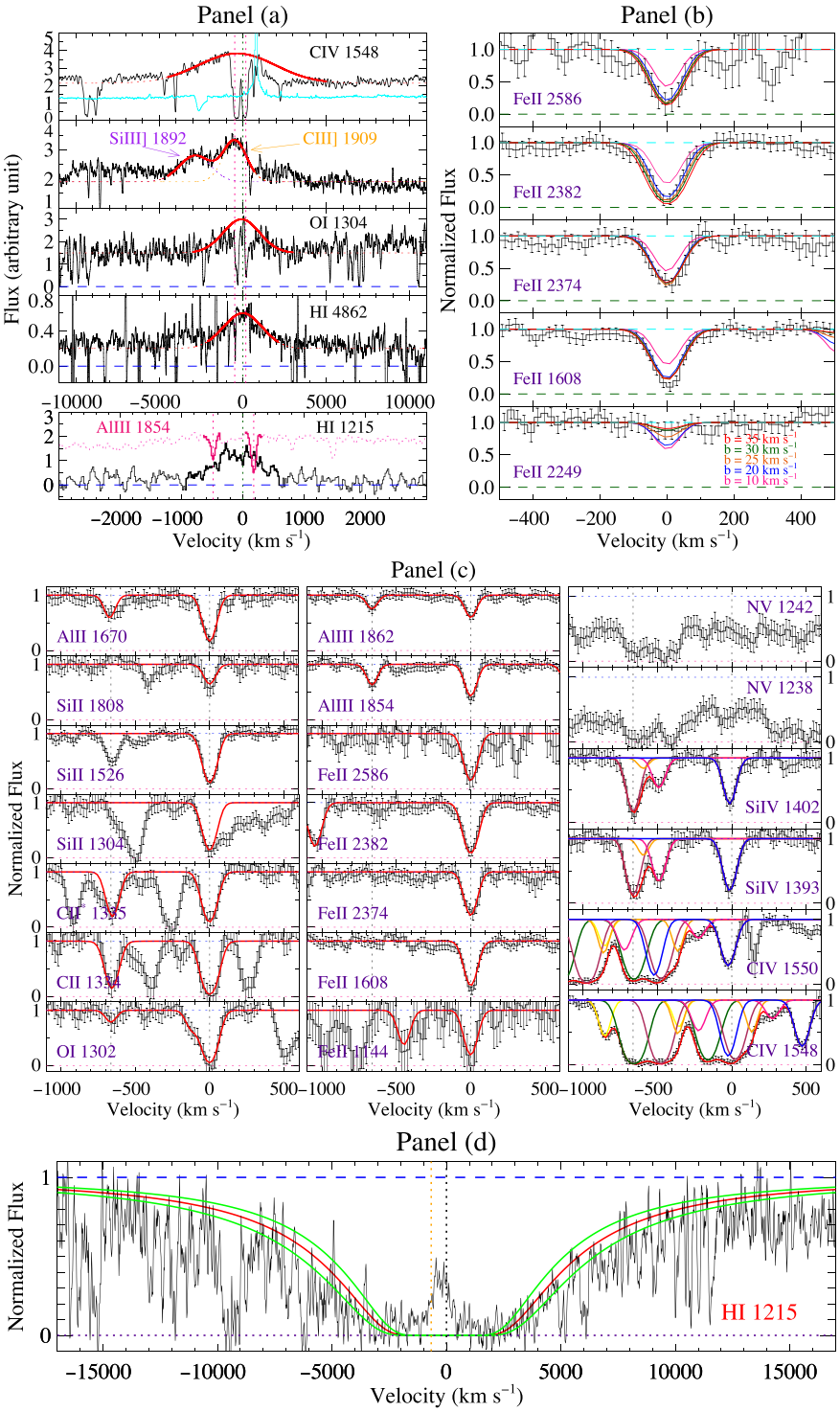

Figure A1. Same as Fig. 1 but for the quasar J0953+0349 with $z_{em} = 2.5940$ and $z_{abs} = 2.5961$. The H I λ 4862 spectrum in panel (a) is from XSHOOTER observation.

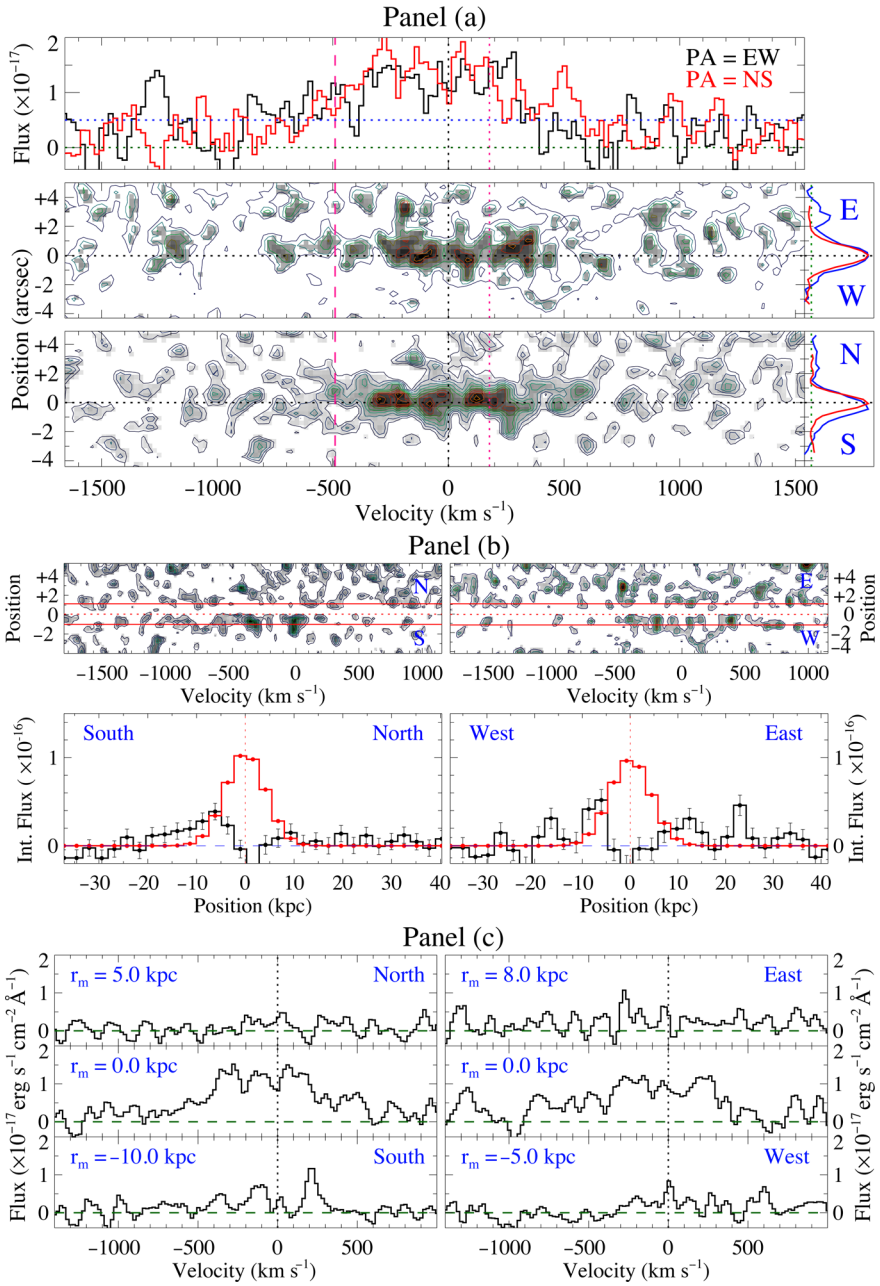

Figure A2. Same as Fig. 2 but for the quasar J0953+0349. The zero velocity is at $z_{em} = 2.5940$. In panel (a), the pink dotted lines mark the position of the DLA at $z_{abs} = 2.5961$ and the pink dashed lines show the position of the absorber at $z_{abs} = 2.5880$. In panels (a) and (b) the outermost contour along PA = NS (resp. PA = EW) corresponds to a flux density of 9.10×10^{-20} (resp. 1.36×10^{-19}) erg s^{-1} cm^{-2}Å^{-1} and each contour is separated by 9.10×10^{-20} (resp. 1.36×10^{-19}) erg s^{-1} cm^{-2}Å^{-1} from its neighbouring contour.

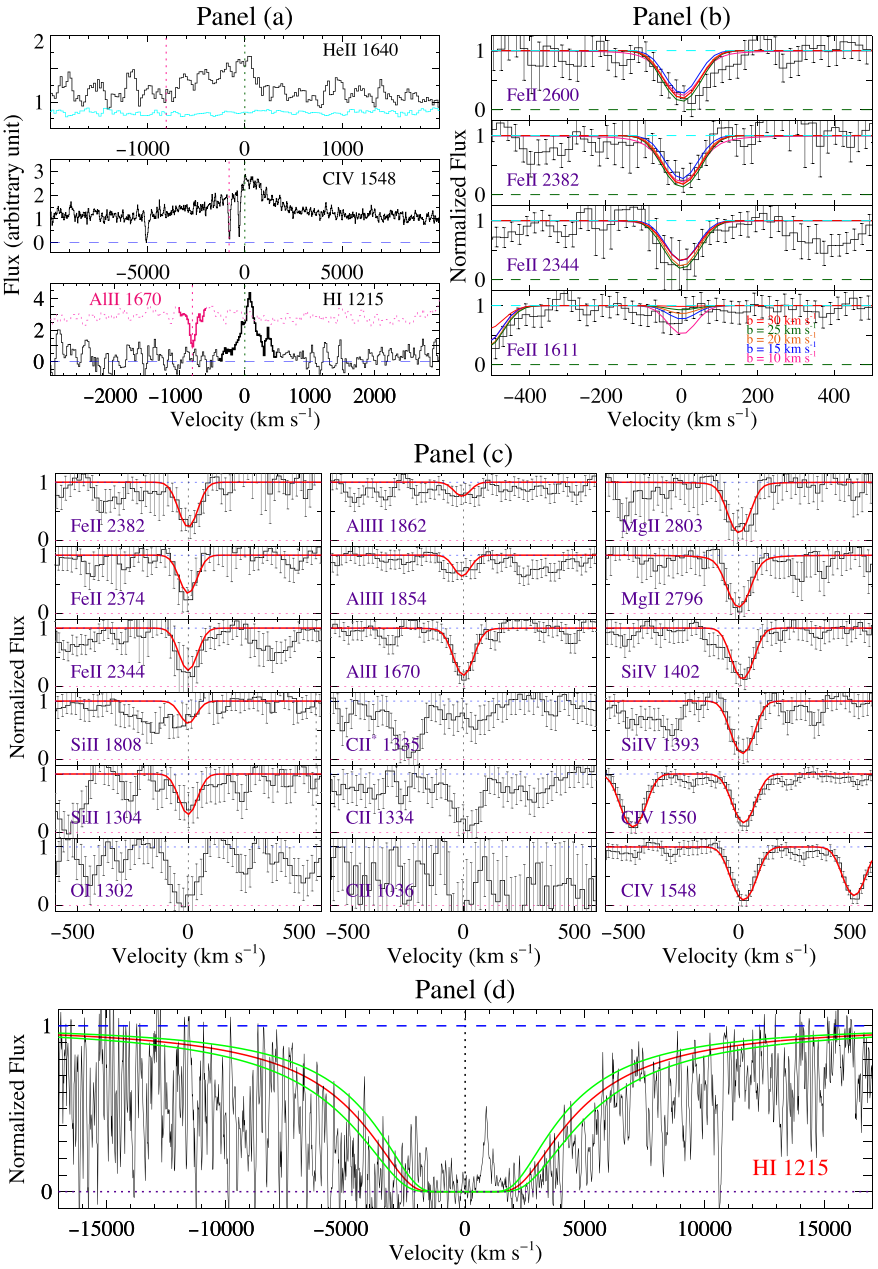

Figure A3. Same as Fig. 1 but for the quasar J1058+0315 with $z_{em} = 2.3021$ and $z_{abs} = 2.2932$.

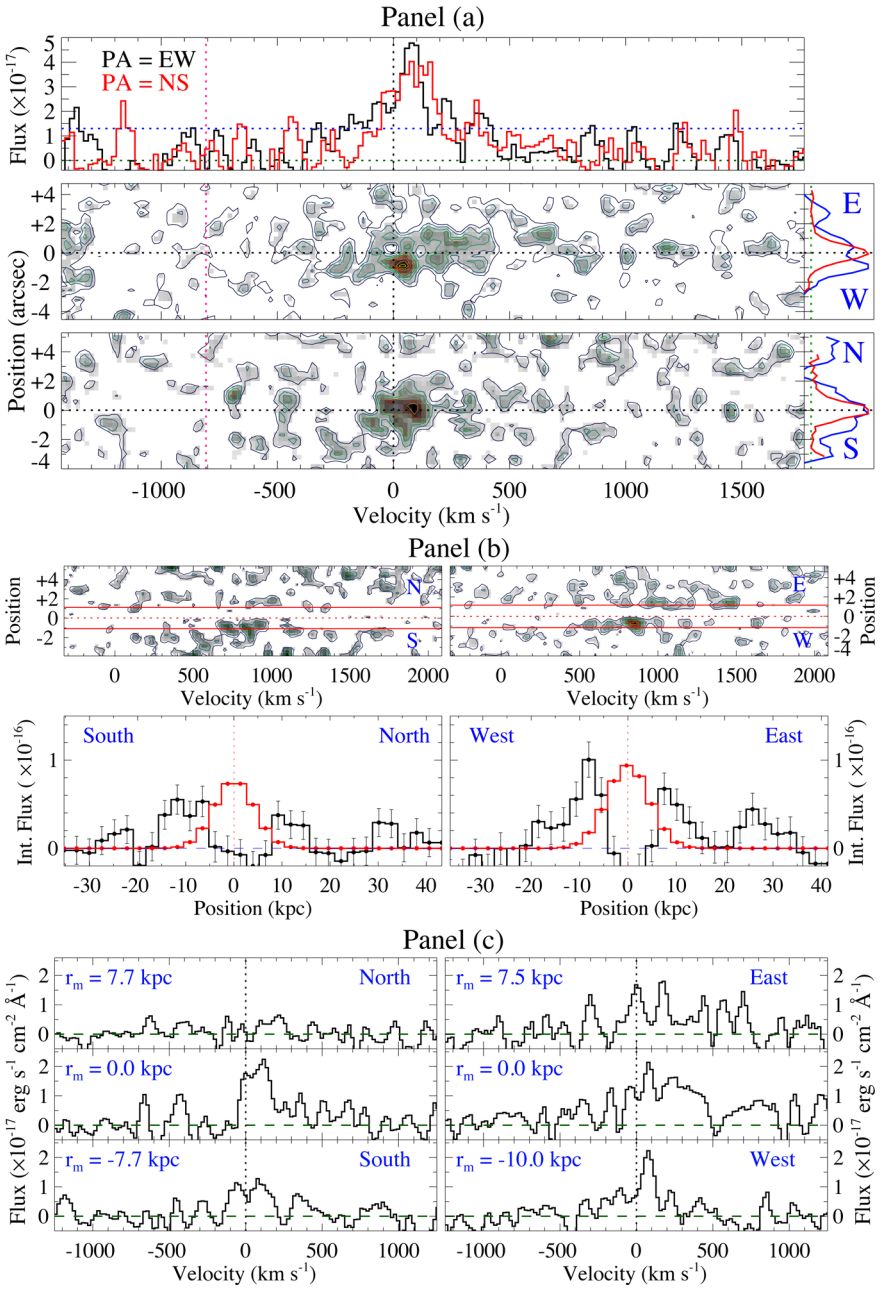

Figure A4. Same as Fig. 2 but for the quasar J1058+0315. The zero velocity is at $z_{em} = 2.3021$. In panel (a), the pink dotted lines mark the position of the DLA with $z_{abs} = 2.2932$. In panels (a) and (b) the outermost contour along PA = NS (resp. PA = EW) corresponds to a flux density of 2.94×10^{-19} (resp. 3.36×10^{-19}) erg s^{-1} cm^{-2} Å^{-1} and each contour is separated by 2.94×10^{-19} (resp. 3.36×10^{-19}) erg s^{-1} cm^{-2} Å^{-1} from its neighbouring contour.

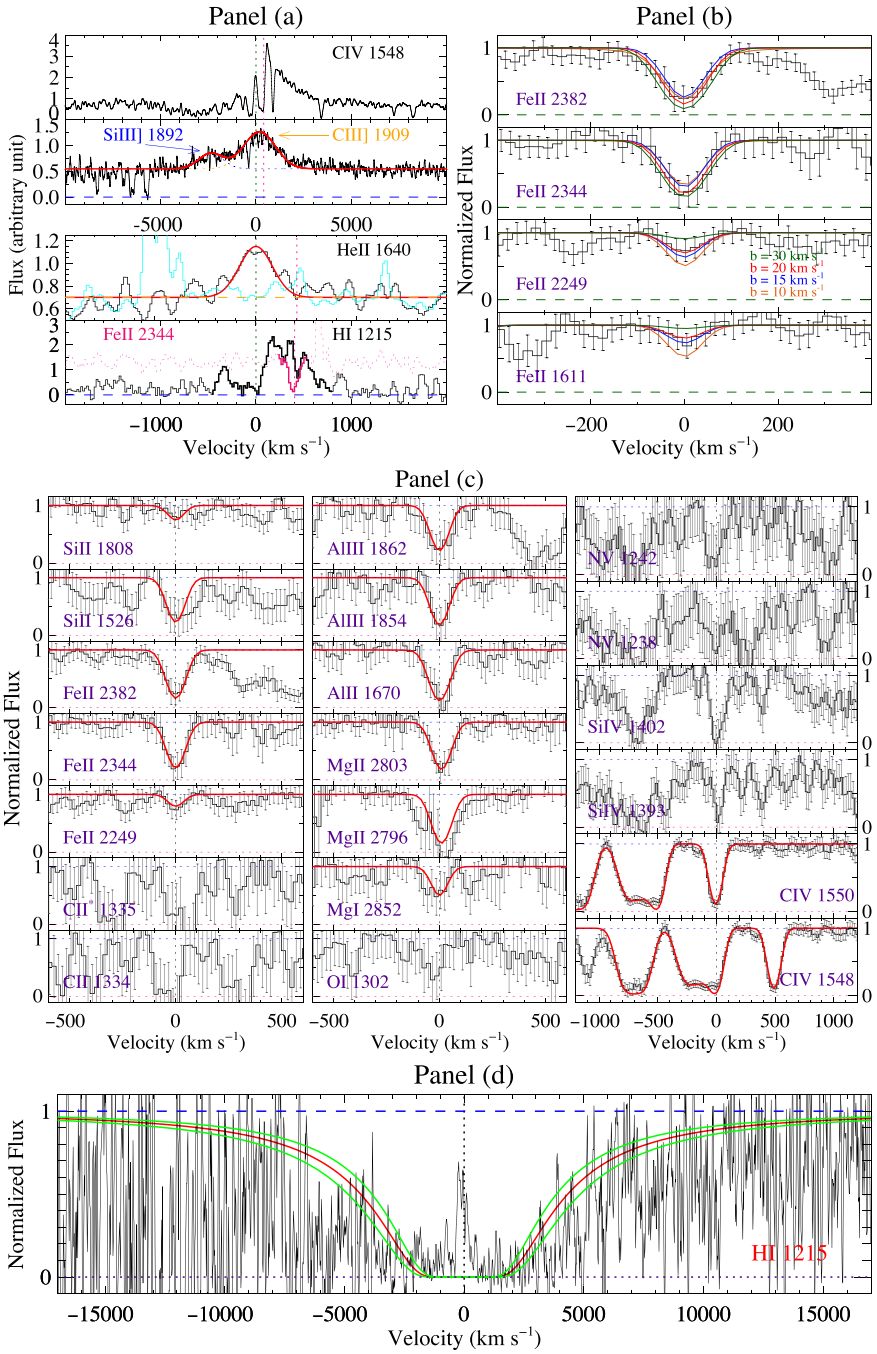

Figure A5. Same as Fig. 1 but for the quasar J1154−0215 with $z_{em} = 2.1810$ and $z_{abs} = 2.1853$.

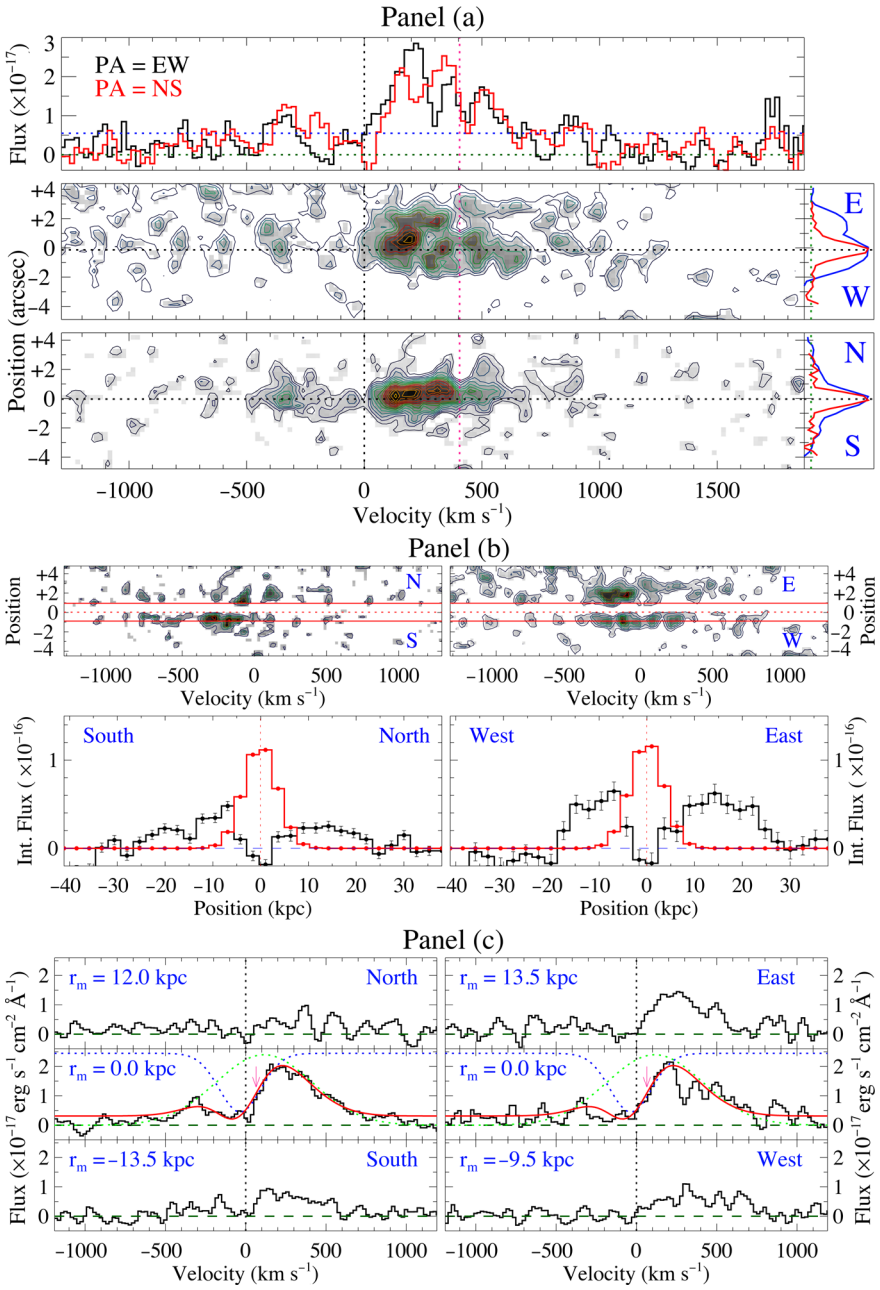

Figure A6. Same as Fig. 2 but for the quasar J1154−0215. The zero velocity is at $z_{em} = 2.1810$. In panel (a), the pink dotted lines mark the position of the DLA with $z_{abs} = 2.1853$. In panels (a) and (b) the outermost contour along PA = NS (resp. PA = EW) corresponds to a flux density of 1.60×10^{-19} (resp. 1.29×10^{-19}) erg s^{-1} cm^{-2} Å^{-1} and each contour is separated by 8.00×10^{-20} (resp. 1.29×10^{-19}) erg s^{-1} cm^{-2} Å^{-1} from its neighbouring contour. See the text for the description of the red solid line, and the blue and green dotted lines shown in panel (c).

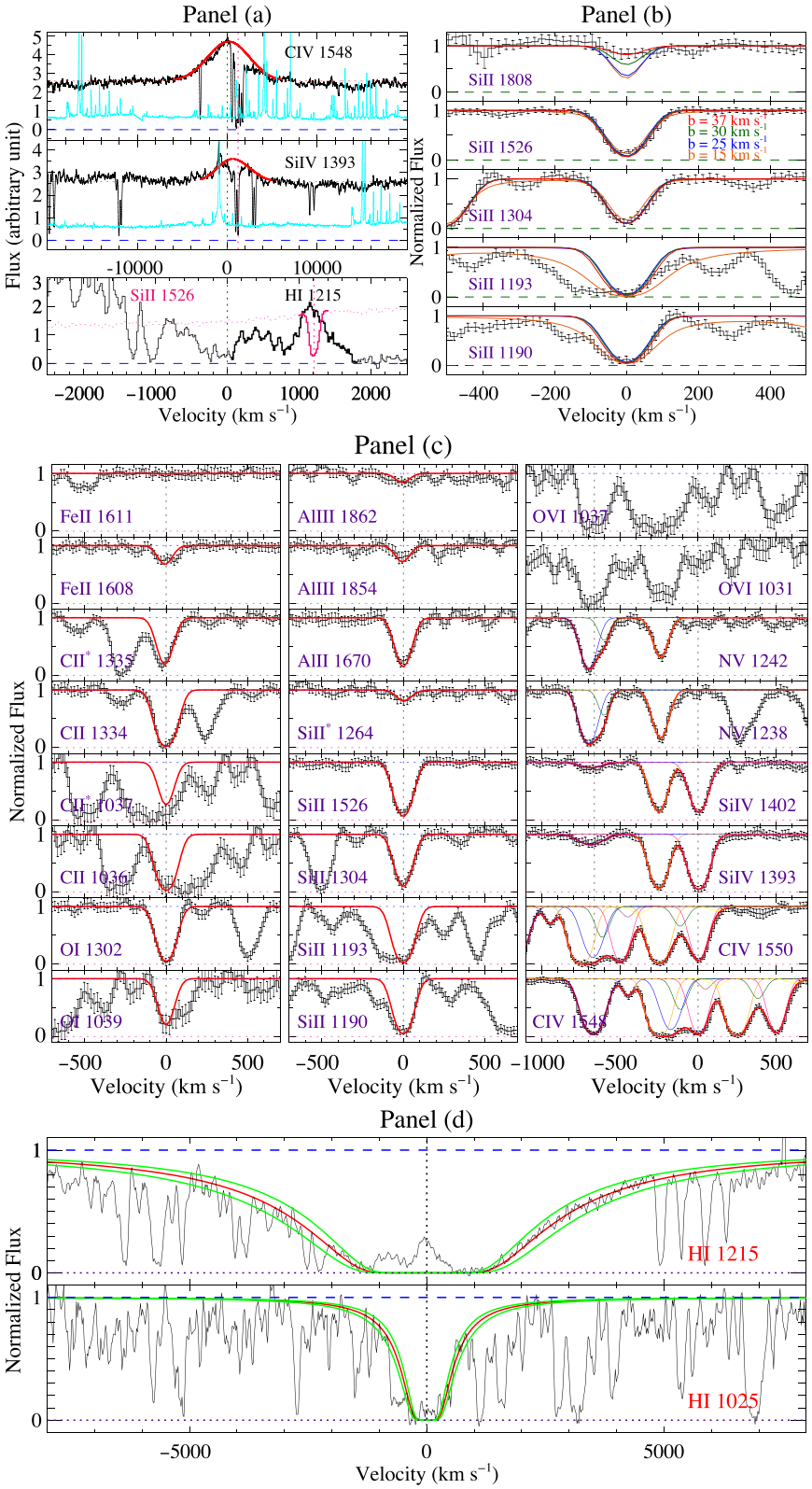

Figure A7. Same as Fig. 1 but for the quasar J1253+1007 with $z_{em} = 3.0150$ and $z_{abs} = 3.0312$.

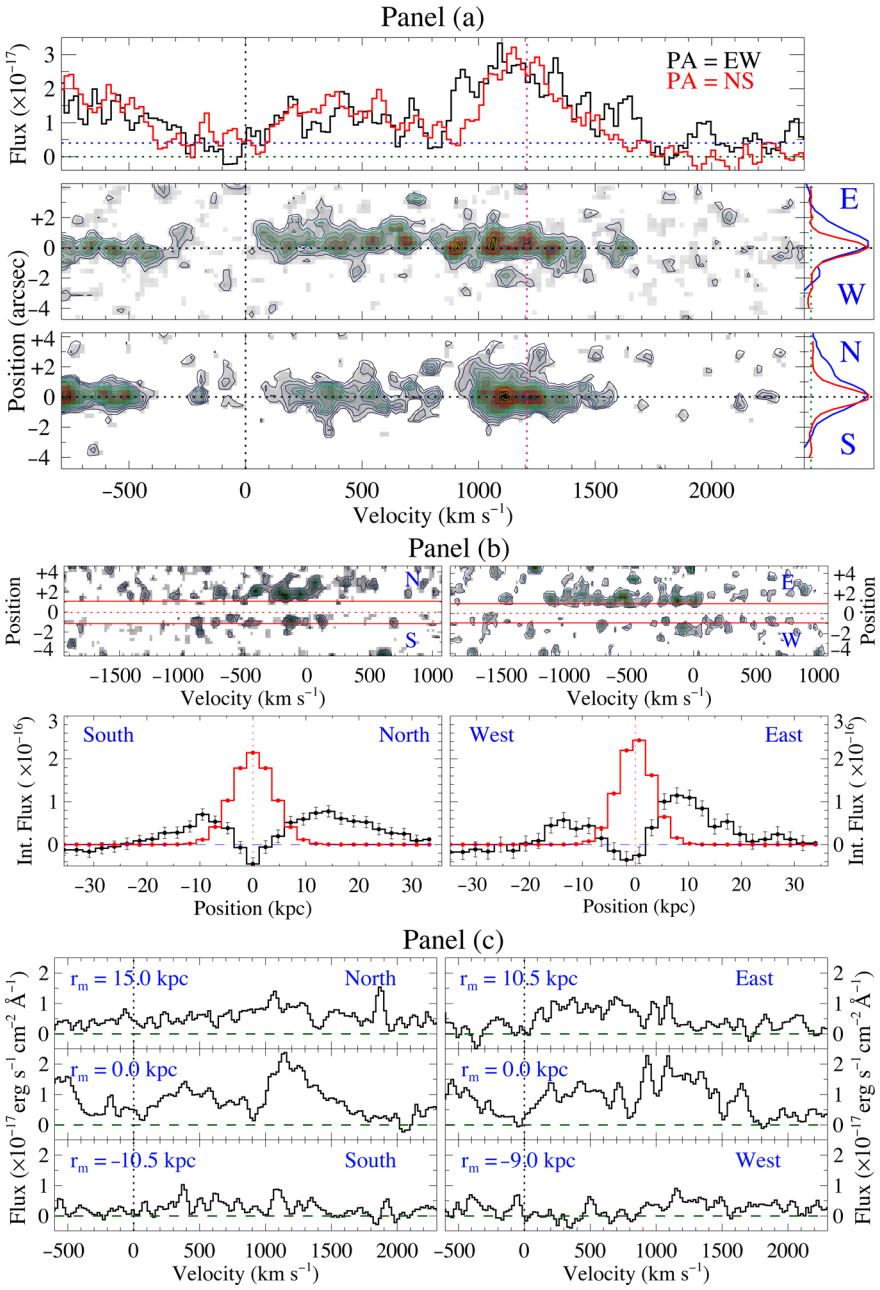

Figure A8. Same as Fig. 2 but for the quasar J1253+1007. The zero velocity is at $z_{em} = 3.0150$. In panel (a), the pink dotted lines mark the position of the DLA with $z_{abs} = 3.0312$. In panels (a) and (b) the outermost contour along PA = NS (resp. PA = EW) corresponds to a flux density of 2.49×10^{-19} (resp. 2.26×10^{-19}) erg s^{-1} cm^{-2} Å^{-1} and each contour is separated by 8.30×10^{-20} (resp. 1.13×10^{-19}) erg s^{-1} cm^{-2} Å^{-1} from its neighbouring contour.

This paper has been typeset from a TEX/LATEX file prepared by the author.